Quality ~~Evaluation of the quality of a UAV-based eddy covariance system~~ Evaluation ~~for measurements~~ for Measurements of ~~w~~Wind ~~F~~field and ~~turbulent flux~~ Turbulent Flux from a UAV-based Eddy Covariance System

Yibo Sun[1,2,3], Bilige Sude[1,2,3], ~~Shaomin Liu[4],~~ Xingwen ~~Lin[5]~~Lin[4], ~~Ziwei Xu[4],~~ Bing ~~Geng[6]~~Geng[5], Bo Liu[1,2,3], Shengnan Ji[1,2,3], Junping ~~Jing[7]~~Jing[6], Zhiping ~~Zhu[8]~~Zhu[7,9][8], Ziwei Xu[9], Shaomin Liu[9]~~Bilige Sude[1,2,3]~~, Zhanjun Quan[1,2,3]

[1]State Key Laboratory of Environmental Criteria and Risk Assessment, Chinese Research Academy of Environmental Sciences, Beijing 100012, China.
[2]Institute of Ecology, Chinese Research Academy of Environmental Sciences, Beijing 100012, China.
[3]State Environmental Protection Key Laboratory of Ecological Regional Processes and Functions Assessment, Beijing 100012, China.
~~[4]State Key Laboratory of Earth Surface Processes and Resource Ecology, Faculty of Geographical Science, Beijing Normal University, Beijing 100875, China.~~
~~[5]Collage~~ [4]State Key Laboratory of Earth Surface Processes and Resource Ecology, Faculty of Geographical Science, Beijing Normal University, Beijing 100875, China.
[4]Collage of Geography and Environment Science, Zhejiang Normal University, Zhejiang 321004, China.
~~[6]Beijing~~ [5]Beijing Academy of Social Sciences, Beijing 100101, China.
~~[7]National~~ [6]National Ocean Technology Center, Tianjin 300112, China.
~~[8]Kunming~~ [7]Kunming General Survey of Natural Resources Center, China Geological Survey, Kunming 650111, China.
~~[9]Technology~~ [8]Technology Innovation Center for Natural Ecosystem Carbon Sink, Ministry of Natural Resources, Kunming 650100, China.
[4][9]State Key Laboratory of Earth Surface Processes and Resource Ecology, Faculty of Geographical Science, Beijing Normal University, Beijing 100875, China.

Correspondence to: ~~Yibo Sun~~Bilige Sude (~~sun.yibo~~sude@craes.org.cn) and Shaoming Liu (smliu@bnu.edu.cn)

Abstract. Instrumentation packages ~~of~~for eddy covariance (EC) measurements have been developed for ~~a small~~ unmanned aerial vehicle (UAV) to measure the turbulent fluxes of latent heat (LE), sensible heat (H), and CO_2 (Fc) in the atmospheric boundary layer. This study aims to ~~evaluates~~ evaluate the ~~measurement~~ performance of this UAV-based EC system. First, the measurement precision (1σ) of geo-referenced wind ~~measurement~~ was estimated at 0.07 m s^{-1}. Then, the effect of calibration parameter and aerodynamic characteristics of the UAV on ~~the quality of the measured~~ wind measurement was examined by conducting a set of calibration flights. The results shown that the calibration improved the quality of measured wind field, and the influence of upwash and leverage effect can be ignored in ~~the~~ wind measurement by the UAV. Third, for ~~the~~ measurement of turbulent ~~fluxes~~ flux, the ~~measurement~~ error caused by instrumental noise was estimated at 0.03 µmol m^{-2} s^{-1} for Fc, 0.02 W m^{-2} for H, and 0.08 W m^{-2} for LE. Fourth, data from the standard operational flights are used to assess the influence of resonance on the measurements and to test the sensitivity of the measurement under the variation (±30 %) of the calibration parameters

around their optimum value~~s~~. Results shown that the effect of resonance mainly affect the measurement of CO_2 (~5 %). The pitch offset angle (ε_θ) significantly affected the measurement of vertical wind (~30 %) and turbulent fluxes (~15 %). The heading offset angle (ε_ψ) mainly affected the measurement of horizontal wind (~15 %), and other calibration parameters had no significant effect on the measurements. The results lend confidence to use the UAV-based EC system, and suggest future ~~directions~~ improvements for optimization ~~and development~~ of the next generation system.

1 Introduction

In environmental, hydrological and climate change sciences, flux measurement ~~the measurement of surface fluxes~~ at the regional scale (level of several to tens of kilometers) ~~has attracted great interest~~ is a pressing problem~~despite often being considered a gordian knot~~ (Mayer et al., 2022; Chandra et al., 2022). Process-based or remote sensing (RS)-based models are often used to estimate land surface fluxes of matter and energy at continental to global scales with typical spatial resolution from 1-10 km (Hu and Jia, 2015; Mohan et al., 2020; Liu et al., 1999). However, observational data, especially at similar scales to models' estimates, is often lacking, which presents a significant challenge for the validation and evaluation of the surface flux products from these models' estimates (Li et al., 2018; Li et al., 2017). On the ground, in the past decades, extensive eddy-covariance (EC) flux sites with their composed networks and optical-microwave scintillometer (OMS) sites have been built to provide temporally continuous monitoring of surface flux at local (hundreds of meters around the measurement site of ground EC) and path (a distance of a few hundred meters to near 10 kilometers between transmitter and receiver terminal of OMS) scales (Yang et al., 2017; Liu et al., 2018; Zhang et al., 2021; Zheng et al., 2023). ~~Generally speaking~~However, flux from ground measurements need to be scaled up to kilometers-scale to provide comparable ~~spatial~~ surface "relative-truth" flux data for the process- or RS-based models at larger spatial scales (Liu et al., 2016). ~~However,~~But the spatial density of these flux measurements sites is still low compared to the heterogeneity of surface fluxes, which means that major scaling bias may exist in the upscaled flux data (Wang et al., 2016; Li et al., 2021). Therefore, regional-scaled oriented flux measurement techniques need to be developed to complement the missing scale between these ground- and models-based approaches (Chu et al., 2021).

Aircraft-based EC flux measurement method, which has been developed for turbulence measurements for more than 40 years (Lenschow et al., 1980; Desjardins et al., 1982), is considered as the optimum method to measure turbulent flux at regional scale (several hundred square kilometers)~~, thus bridging the scale gap between ground and model-derived methods~~ (Gioli et al., 2004; Garman et al., 2006). To date, several types of aircrafts, including manned or unmanned fixed-wing aircrafts, delta-wing aircrafts, and helicopters, have been used for measurements of turbulent flux by equipping them with the EC sensors to measure three-dimensional (3D) wind, air temperature, and gas concentrations at a high frequency ~~of 50 Hz~~ (Gioli et al., 2006; Metzger et al., 2012; Wolfe et al., 2018; Sun et al., 2021a; Reuter et al., 2021). Among them, fixed-wing aircrafts and delta-wing aircrafts are better airborne platforms for EC measurements compared to helicopters due to their tightly coupled structure with the wind sensor and because their flow distortion around the fuselage can be more easily avoided or modeled (Prudden et al., 2018; Garman et al., 2008). A wide range of manned aircrafts has been developed to measure turbulent flux,

including single-engine light aircrafts (e.g., Sky Arrow 650, Long-EC, WSMA) (Gioli et al., 2006; Crawford and Dobosy, 1992; Metzger et al., 2012), twin-engine aircrafts (e.g., Twin Otter, NASA CARAFE) (Desjardins et al., 2016; Wolfe et al., 2018) and larger quad-engine utility aircrafts (e.g., NOAA WP-3D) (Khelif et al., 1999). These airborne flux measurements, in combination with ground EC measurements, provide an excellent opportunity to produce regional-scaled, spatio-temporal continuous surface flux datasets that can improve our understanding of the processes of land-atmosphere interactions in regional and global change (Chen et al., 1999; Prueger et al., 2005; Calmer et al., 2019; Tadić et al., 2021). However, manned aircrafts are expensive to operate and maintain. Aviation safety and operational regulations require that manned aircrafts must fly above a minimum altitude (400 m above the highest elevation within 25 km on each side of the center line of the air route in China) and must avoid hazardous conditions such as icing or severe turbulence. The flow distortion induced by the aircraft itself (from the wings, fuselage, and the propellers) complicates the wind vector measurement from aircraft platform, which means that sophisticated correction procedures should be applied to ~~compensate~~ correct for the flow distortion effects (Elston et al., 2015; Williams and Marcotte, 2000; Drüe and Heinemann, 2013).

In recent years, interesting in unmanned aerial vehicle (UAV) platforms for atmospheric research ~~studies~~ have been fast growing, especially because of their lower construction, operation, and maintenance costs compared with manned platforms. High-performance fixed-wing UAVs offer a high payload capacity (5-10 kg) and similar endurance (2-3 h) and operating altitude (~~up~~ to 3500 m or higher above the sea level) to manned aircrafts, but with much less turbulence disturbance due to their small fuselage size (Reineman et al., 2013). More importantly, the advancements in small, fast, and powerful sensors and microprocessors make it possible to use of UAVs for comprehensive atmospheric measurements (Sun et al., 2021a). Several types of UAVs with different ~~turbulence~~ atmospheric measurement objectives have been developed and deployed, ranging from small ~~payload capacity~~ size (e.g., 140 g SUMO) to medium (e.g., 1.5 kg M²AV, 1.0 kg MASC) and large (e.g., 6.8 kg Manta, 5.6 kg ScanEagle) (Reuder et al., 2016; Båserud et al., 2016; Reineman et al., 2013; Zappa et al., 2020). A comprehensive overview of ~~the use of~~ these UAVs for ~~turbulence sampling~~ atmospheric measurement can be found in Elston et al. (2015) and Sun et al. (2021a). For turbulence measurement~~s~~, the UAVs were equipped with a commercial or custom multi-hole (5- or 9-hole) probe paired with an integrated navigation system (INS) to obtain the wind vector. Small and medium UAVs typically could only measure fast 3D wind vector and air temperature fluctuations for measurements of momentum and sensible heat flux, whereas, large UAVs were equipped with more types (e.g., radiation, optics, or gas concentration) and more accurate sensors for measurement of ~~a larger range of~~ more types of meteorological properties including sensible and latent heat fluxes, CO_2 flux, radiation fluxes as well as surface properties (Reineman et al., 2013; Sun et al., 2021a). UAVs ~~equipped with scientific instruments~~ can be deployed in a variety of application environments and complex conditions~~.~~ ~~UAVs,~~ which offer distinct advantages over manned aircraft in their ability to safely perform measurements in low-altitude conditions (below 100 m above the ground level) and greatly reduce operational costs ~~especially in low-altitude conditions (below 100 m above the ground level), which are optimal for measuring turbulent flux~~ (Witte et al., 2017). Anderson and Gaston (2013) predict that UAVs will revolutionize the spatial data collection in ecology and meteorology.

设置了格式: 字体颜色: 自动设置

102 EC method is a well-developed technology for directly measuring vertical turbulent flux (flux of sensible heat, latent heat
103 and CO_2) within the atmospheric boundary layers (ABL) (Peltola et al., 2021). It requires accurate time (for ground tower) or
104 spatial (for mobile platform) series of both the transported scalar quantity and the transporting turbulent wind. Each should be
105 measured at sufficient frequency to resolve the flux contribution from small eddies (Vellinga et al., 2013). However, ~~T~~the
106 measurement of the geo-referenced 3D wind vector, which is the prerequisite for EC measurements, is challenging for airborne
107 platform. ~~Airborne measurement of~~The geo-referenced 3D wind measured by airborne is the vector sum between the aircraft
108 velocity relative to the earth (inertial velocity) and the velocity relative to the air (relative wind vector, or true airspeed).
109 Therefore, accurate measurements of the relative wind as well as the motion and attitude of the platform are essential to
110 accurately measure the geo-referenced wind vector and the turbulent flux (Metzger et al., 2011). Garman et al. (2006) estimated
111 the measurement precision (1σ) of the vertical wind measurements of a commercial 9-hole turbulence probe (known as "Best
112 Air Turbulence Probe", often abbreviated as the "BAT Probe") to be 0.03 m s^{-1} by combining the precision of the BAT Probe
113 and the integrated navigation ~~device~~system. ~~The BAT Probe is widely used on manned fixed-wing aircrafts, such as Sky Arrow~~
114 ~~650 ERA (Environmental research aircraft), Beechcraft Duchess, and Diamond DA42, for turbulent flux measurement~~ A light
115 delta-wing EC flux measurement aircraft developed by Metzger et al. (2011) reported a 1σ precision of wind measurement of
116 0.09 m s^{-1} for horizontal wind and 0.04 m s^{-1} for vertical wind using a specially customized five-hole probe (5HP). On this
117 basis, in combination with a commercial infrared gas analyzer, the 1σ precision of flux measurement was 0.003 m s^{-1} for
118 friction velocity, 0.9 W m^{-2} for sensible heat flux, and 0.5 W m^{-2} for latent heat flux (Metzger et al., 2012). The EC flux
119 measurement from a UAV platform can now be achieved with a similar reliability to a manned platform. The Manta and
120 ScanEagle UAV-based EC measurements developed by Reineman et al. (2013) achieved precise wind measurements (0.05 m
121 s^{-1} for horizontal and 0.02 m s^{-1} for vertical wind) using a custom nine-hole probe and a commercial high precision integrated
122 navigation system (INS)~~, at a lower price and lighter weight than the commercial BAT probe~~. However, the onboard instrument
123 packages for Manta and ScanEagle UAV are independent of each other in their measurements of turbulent and radiation flux,
124 and the CO_2 flux measurement is lacking.
125 Inspired by these studies, Sun et al. (2021a) used a high-performance fuel-powered vertical take-off and landing (VTOL)~~,~~
126 fixed-wing UAV platform to integrate the scientific payloads for EC and radiation measurements to obtain a comprehensive
127 measurement of turbulent and radiation flux ~~using an UAV~~. This UAV-based EC system could ~~measure~~measured turbulent
128 fluxes of sensible heat, latent heat, and CO_2, as well as radiation fluxes including net radiation and upward- and downward-
129 looking photosynthetically active radiation (PAR). This system was successfully tested in the Inner Mongolia of China and
130 applied to measure the regional sensible and latent heat fluxes in the Yancheng coastal wetland in Jiangsu, China (Sun et al.,
131 2021a; 2021b). During these field studies, the UAV-based EC measurements achieved a near consistent observational result
132 compared with ground EC measurements (Sun et al., 2021b). However, some shortcomings in the developed UAV-based EC
133 system were also identified. In particular, the noise effects from the engine and propeller were not fully isolated, resulting in
134 high frequency noise in the measured scalars (air temperature, H_2O, and CO_2 concentration). This UAV-based EC system is
135 being continuously improved (in Section 2.1) ~~based on field measurements~~. However, ~~there is~~ no quantitative evaluation of

136 the measurement precision of the wind field and turbulent flux as well as of the influence of the resonance noise from the UAV

137 operation have been made yet. Previous work using ground EC as a benchmark to assess the measurement performance of the

138 UAV-based EC system has been disputed, due to difference in EC sensors, platforms, measurement height, and source areas

139 (i.e., footprint), as well as the influence of surface heterogeneity, flux divergence, inversion layer and the stochastic nature of

140 turbulence (Sun et al., 2021b; Wolfe et al., 2018; Hannun et al., 2020).

141 This study attempts to evaluate the performance of the UAV-based EC system developed by Sun et al. (2021a) in the

142 measurement of wind field and turbulent flux. For these purposes, data from two field measurement campaigns, including a

143 set of calibration flights and some standard operation flights, were used in this study. First, the current study investigated the

144 quality of the measurement of geo-referenced wind vector including measurement error (1σ) and the improvements for wind

145 measurement after system calibration. Second, using the measured data from standard operation flights, flux measurement

146 error related to instrumental noise was estimated with a method proposed by Billesbach (2011). Errors propagated through the

147 correction terms [i.e., Webb-Pearman-Leuning (WPL) correction for latent heat and CO_2 flux] were also included in our

148 analysis (Webb et al., 1980; Kowalski et al., 2021). Then, the impacts of resonance noise on the measured scalar variance and

149 the flux covariance were also estimated by comparing the real (co)spectra curve with the theoretical reference curve from

150 Massman and Clement (2005). Lastly, the sensitivity of the measured geo-referenced wind vector and turbulent flux to the

151 errors in the calibration parameters (determined by the calibration flight) were assessed by adding an error of ±30 % to their

152 optimum calibrationcalibrated value.

2 Materials and Methods

2.1 The UAV-based EC system

155 The VTOL fixed-wing UAV platform used for EC measurement is a high-performance, fuel-powered VTOL, fixed-wing UAV,

156 which has minimal requirements for the takeoff location and offers a high payload capacity of up to 10 kg. Thise UAV has a

157 wing-span of 3.7 m, a fuselage length of 2.85 m, and a maximum take-off weight of 60 kg. The UAV engine is mounted in a

158 pusher configuration, allowing for the turbulence probe to be installed directly on the nose of the UAV, minimizing or

159 eliminating airflow contamination due to upwash and sidewash generated by the wings (Crawford et al., 1996). Control of the

160 UAV is totally autonomous, and the pilots have the option to enable manual and semi-manual control in emergency conditions.

161 The UAV has a cruise flight speed of 28 to 31 m s^{-1} with an endurance of almost 3 h, and it has a flight ceiling of up to 3800

162 m above the sea level. Detailed information on about this UAV could be found in Sun et al. (2021a).

163 The flux payloads of the UAV-based EC system include a precision-engineered 5-hole pressure probe (5HP) for

164 measurement of the true airspeed and the attack (α) and sideslip (β) angles of the incoming flow relative to the UAV, a dual-

165 antenna integrated navigation system (INS) for high accuracy measurement of UAV ground speed and attitude, an open path

166 infrared gas analyzer (IRGA) for recording the atmospheric gas densities concentrations of CO_2 and water vapor, a fast

167 temperature sensor for measurement of the fast temperature fluctuations, and a slow-response temperature probe for providing

168 a mean air temperature reference. The sensor modules and their 1σ precision of the measured variables related to EC
169 measurement were listed in Table 1. For the 5HP, the 1σ measurement precision was acquired from the wind tunnel test after
170 wind tunnel calibration (Sun et al., 2021a).

171 **Table 1**: Summary of the sensor modules, measured variables, and their measurement precision used to determine the geo-
172 referenced wind velocity and turbulent flux.

Sensor (Module, company, country)	Variables	Precision (1σ)
GNSS/INS (BD992-INS, Trimble, USA)	Roll, Pitch, Heading	0.1º
	Horizontal velocity	0.007 m s^{-1}
	Vertical velocity	0.02 m s^{-1}
5HP (ADP-55, Simtec AG, Switzerland)	Attack angle	0.02º[#]
	Sideslip angle	0.04º[#]
	True airspeed	0.05 m s^{-1}[#]
	Static pressure	1.1 hPa
	Dynamic pressure	0.003 hPa
IRGA (EC150, Campbell, USA)	CO_2 density	0.2 mg m^{-3}
	H_2O density	0.004 g m^{-3}
Thermistor (100K6A1IA, Campbell, USA)	Temperature (slow)	0.2 ℃
Thermocouple (T-type COCO-003, Omega, USA)	Temperature (fast)	0.5 ℃

173 [#] Results from the wind tunnel test.

174 The sample rate of EC measurement is 50 Hz except for the slow-response temperature probe (1 Hz), yielding a turbulence
175 horizontal resolution of approximately 1.2 m at a cruising speed of 30 m s^{-1}. The system was improved according to deficiencies
176 identified after several field measurements with the following adjustments: 1) a laser distance measurement unit was mounted
177 for measuring the distance between the UAV and the ground level, 2) the platinum resistance thermometer was replaced by a
178 thermocouple (Omega T-type COCO-003; Ø0.075 mm) for improving the resistance of the high-frequency temperature
179 measurements to vibration noise from the engine, 3) the vibration isolator structure of the IRGA was improved, and 4) the
180 original datalogger (CR1000X, Campbell, USA) was replaced with a lighter one (CR6, Campbell, USA). All the digital and
181 analog signals from the sensor modules are stored and synchronized by the on-board datalogger, and the on-board scientific
182 payloads are designed to be isolated from the electronic components of the UAV to ensure that any problems occurring would
183 not jeopardize the safety of the UAVflying (Sun et al., 2021a).

184 In the present study, to estimate the measurement precision of the geo-referenced wind and turbulent flux, the sensor
185 modules and their 1σ precision of the measured variables related to EC measurement were used, as presented in Table 1. For
186 the 5HP, the 1σ measurement precision was acquired from the wind tunnel test after wind tunnel calibration (Sun et al., 2021a).

187 **Table 1**: Summary of the sensor modules, measured variables, and their measurement precision used to determine the geo-
188 referenced wind velocity and turbulent flux.

Sensor (Module, company, country)	Variables	Precision (1σ)
GNSS/INS (BD992-INS, Trimble, USA)	Roll, Pitch, Heading	0.1°
	Horizontal velocity	0.007 m s^{-1}
	Vertical velocity	0.02 m s^{-1}
5HP (ADP-55, Simtec AG, Switzerland)	Attack angle	0.02°#
	Sideslip angle	0.04°#
	True airspeed	0.05 m s^{-1}#
	Static pressure	1.1 hPa
	Dynamic pressure	0.003 hPa
IRGA (EC150, Campbell, USA)	CO_2 density	0.2 mg m^{-3}
	H_2O density	0.004 g m^{-3}
Thermistor (100K6A11A, Campbell, USA)	Temperature (slow)	0.2 °C
Thermocouple (T type COCO-003, Omega, USA)	Temperature (fast)	0.5 °C

189   # Results from the wind tunnel test.

190   **2.2 Field campaign**

191   **2.2.1 In-flight calibration campaign**

192   In order to calibrate the ~~wind measurement component~~mounting error in 5HP of the UAV-based EC system, an in-flight

193   calibration campaign was carried out on 4 September 2022 at the Caofeidian Shoal Harbor in the Bohai Sea of northern China.

194   ~~The average water depth of this area is approximately 0-5 m, with a maximum water depth of 22 m.~~ At low tide, a large area

195   of the tidal flat is exposed; while at high tide, only the barrier islands are visible (Xu et al., 2021). The assumption~~s~~ conditions

196   should be satisfied for calibration flight includ~~ing~~e 1) low turbulent transport condition (i.e., no disturbance), 2) a constant

197   mean horizontal wind, and 3) mean vertical wind near zero (Drüe and Heinemann, 2013; Vellinga et al., 2013; Van Den

198   Kroonenberg et al., 2008). This allows identical wind components for several consecutive straights in opposite or vertical flight

199   directions. These assumptions are usually well satisfied above the ABL or under stable atmospheric conditions (Drüe and

200   Heinemann, 2013). Over the sea surface, due to its uniform and cool surface property, the turbulence fluctuations are weaker

201   than that over the land surface (Mathez and Smerdon, 2018), making where a more ideal environment to conduct calibration

202   flight.

203   The in-flight calibration campaign in this study included three flight maneuvers~~, including~~: ~~a~~ 'box' maneuver, 'racetrack'

204   maneuver, and 'acceleration-deceleration' maneuver. The ~~trajectory~~ trajectories of ~~the calibration flight~~these flight maneuver

205   ~~is~~ are shown in Figure 1~~, with different color corresponding to different flight maneuver~~. The calibration flight was executed

206   between 7:28 a.m. ~~and~~ 7:48 a.m. (~~China Standard Time, CST~~Beijing time) ~~to coincide with the ebb tide stage. During this~~

207   ~~time, the average water depth was approximately 1.1 m~~, and the average~~d~~ flight altitude was 400 m ($\sigma = \pm0.78$ m) above the

208   sea level. Considering the uniform and cool underlying surface and the stable atmospheric conditions ~~in~~ of the early morning,

209 we assume no disturbance from the underlying surface was present during the calibration flight and the assumptions for
210 calibration flight are satisfied.
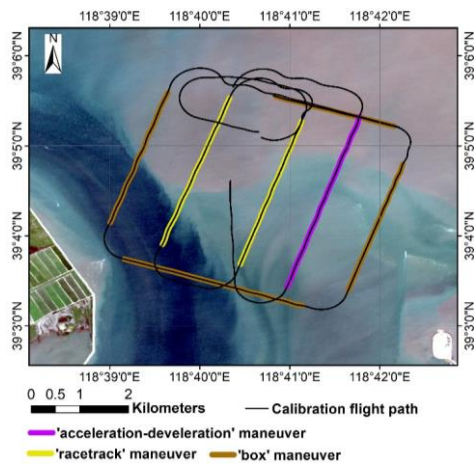
211
212 **Figure 1. Flight trajectoriesy of the calibration flight campaign carried out on 4 September 2022 at the Caofeidian Shoal Harbor in**
213 **the Bohai Sea of northern China. The land surface image is from Sentinel-2A satellite image with true color combination acquired**
214 **on 1 September 2022.**

215 In this study, tThe 'box' maneuver (gray line in Fig. 1) is used to determine the mounting misalignment angle in the heading
216 (ϵ_ψ) and pitch (ϵ_θ) between the 5HP and the center of gravity (CG) of the UAV. The flight path is a box in which the four
217 straight legs are flown at constant cruising speed, flight altitude, and heading continuous for 2 minutes. The 'racetrack'
218 maneuver (yellow line in Fig. 1) is used to evaluate the quality of the calibration parameters acquired from the previous 'box'
219 maneuver. The flight path consists of two parallel straight flight tracks connected by two one 180° turns. Each straight flight
220 section lasts 2 minutes at constant speed and flight altitude. Lastly, the 'acceleration-deceleration' maneuver (purple line in
221 Fig. 1) is used to check the influence of lift-induced upwash from the wing to the measured attack angle by the 5HP. During
222 this maneuver, the aircraft is kept straight and level at constant pressure altitude. When beginning this maneuver, the aircraft
223 accelerates to its maximum airspeed (35 m s^{-1}). Then, the airspeed reduces gradually to near its minimum airspeed (25 m s^{-1})
224 and back up to its maximum airspeed. The pressure-altitude of the aircraft is maintained throughout this maneuver, and the
225 entire maneuver lasts one minute. This maneuver creates a series continuous changed pitch (θ) and attack (α) angle. A If a
226 relationship between the measured incident flow attack angles (α) by the 5HP and the measured pitch angle by the INS of
227 close to 1:1, then it indicates that the effect from the fuselage-induced flow distortion on the wind measurements is negligible
228 (Garman et al., 2006).

229 **2.2.2 Standard operation flight campaign**

230 The reliability of the EC measurement from UAV is susceptible to several factors, mainly including instrumental noise,

231 resonance noise, and the quality of the calibration parameter, etc. In order to evaluate the flux measurement error related to

232 instrumental noise, the effects of resonance on the measured scalar and to investigate the sensitivity of the measured geo-

233 referenced wind vector and turbulent flux to uncertainty in the calibration parameter, we used data from 7 flights in the Dagang

234 district in Tianjin, China between 8 and 16 August 2022. This area is located on the west coast of the Bohai Sea and is a coastal

235 alluvial plain with altitudes between 1-3 m (Chen et al., 2017). The flight path, shown in Figure 2, includes three parallel

236 transect lines of approximately 4 km in length each and at 1-2 km intervals. All flights occurred during the daytime, and were

237 performed in the same trajectory at a low altitude about 90 m above sea level. The flight area covered three different underlying

238 surface types: land, coastal zone, and water surfaces, that can represent typical flux intensity characteristics over different

239 surface conditions.
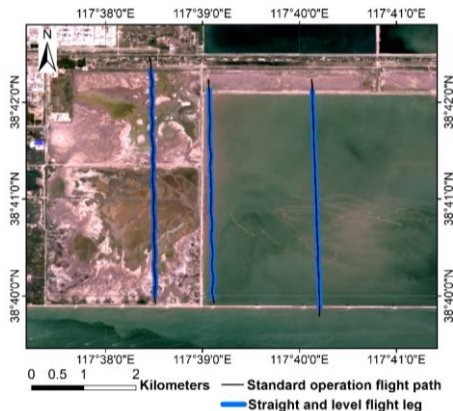
240

241 **Figure 2. Flight trajectories of the standard operation flight campaign carried out between 8 and 16 August 2022 at Dagang**
242 **district, Tianjin, China. The land surface image is from Sentinel-2A satellite image with true color combination acquired on 27**
243 **August 2022.**

244 During the standard operation flight campaign, the atmospheric stability changed from the stable (Monin-

245 Obukhov stability parameter, $z/L = 1.93$) to very unstable ($z/L = -10.28$) conditions as measured by the UAV, where z is

246 the flight height above the ground level, L is the Obukhov length. The stable condition mostly occurred on flight path located

247 over the sea surface, while the unstable condition mostly occurred on flight path located over the land surface. These flight

248 data provided various measurement conditions for us to evaluate the performance of the developed UAV-based EC system.

2.3 Data processing

The raw data collected with the on-board datalogger (CR6, Campbell, USA) is subsequently saved in Network Common Data Form (netCDF) format. It includes dynamic and static pressure, attack, and sideslip angle of incoming flow; slow (1 Hz) and fast (50 Hz) air temperature; mass concentration of H_2O and CO_2; as well as the full navigation data (including 3D location, ground speed, angular velocity, and attitude, etc.) of the UAV. The subsequent data processing includes three ~~basic processing~~ stages in order to calculate flux data from raw measured data.

In the first stage, a moving average filter was used to detect outliers in each variable. Detected outliers were removed and replaced by values obtained by linear interpolation. Outliers tend to be rare. However, if outliers constitute more than 20 % of the data points, the corresponding flight data should be discarded. ~~The cleaned raw data was then used to calculate the geo-referenced wind vector, (co)spectra, and turbulent fluxes.~~

In the second stage, geo-referenced 3D wind vector is calculated. The full form of the equations ~~of motion~~ for calculating the geo-referenced wind vector by the UAV-based EC system is described in detailed in Supplement Part A. From the ~~aircraft~~ airborne platform, geo-referenced wind vector is measured in two independent reference coordinate systems: the relative true airspeed ($\widehat{U}_a$) measurement in the aircraft coordinate system and the ground speed of the aircraft (U_p) in the geo-referenced coordinate system. The geo-referenced wind (U) is the vector sum of the relative true airspeed ($\widehat{U}_a$), the UAV's motion (U_p) and the tangential velocity due to the rotational motion of the aircraft ("lever arm" effect), which is described in Eq. (S2). In this stage, the acquired calibration parameters (ϵ_ψ and ϵ_θ) from the calibration flight are substituted into the Eq. (S8) to correct the mounting angle offset errors between the 5HP and the CG of the UAV. The final equations for geo-referenced wind vector calculation (Eqs. S15 to S17) revealed that the lever arm effects due to the spatial separation between the tip of the wind probe and the CG of UAV ~~can~~may influence the wind measurements. Typically, the separation distance (L) is small, and the influence of the lever arm effects can be ignored when the L is less than about 10 m (Lenschow, 1986). In the current UAV-based EC system, the displacements of the 5HP tip with respect to the CG of the UAV along the three axes of UAB body coordinate are: $x^b = 1.459$ m, $y^b = 0$ m, and ~~x~~$z^b = 0.173$ m (in Supplement Part A). Therefore, in practice, the influence of leverage effects in geo-referenced wind calculation was also ignored in this study. This was also confirmed by assessing the difference in the geo-referenced wind vector with and without the leverage effect correction term in this study (in Section 3.1).

In the final stage, based on the EC technology and spatial averaging, ~~the~~ turbulent flux~~es is~~es are calculated using the covariances of vertical wind (w) with air temperature (T_a) for sensible heat flux (H), with water vapor density (q) for latent heat flux (LE), and with CO_2 density (c) for CO_2 flux (F_c), and with the necessary correction (Webb et al., 1980). The time lag due to the separation between the 5HP tip, the adjacent temperature probe, and the open-path gas analysis did not need to be corrected because the time delay was ~~less than 1 second~~very small at the cruise airspeed of 30 m s^{-1} and sensor separation less than 20 cm. Only the measurement data from the straight-line portion of the flight path ~~can be~~was used in flux calculation. Detailed calculation procedure and formulas ~~of~~ for calculating H, LE, and F_c used by the ~~present~~ current UAV-based EC system are provided in Supplement Part B, including spatially averaging, coordinate rotation, and necessary correction (i.e.,

282 WPL correction for LE and F_c). In this study, the entire measured data of each straight and level flight leg (each with length
283 about 4 km) from the standard operational flight campaign was used to calculate turbulent flux, regardless of the uncertainty
284 in fluxes associated with spatial averaging.

285 ~~One important aspect for airborne EC measurement is the definition of a proper spatial averaging length to calculate~~
286 ~~turbulent flux . Such spatial averaging length depends on the flying altitude, surface characteristics, and atmospheric stability,~~
287 ~~and could be determined using Ogive analysis (Gioli et al., 2004). In this study, the entire measured data of each straight and~~
288 ~~level flight leg (each with length about 4 km) from the standard operational flight campaign was used to calculate turbulent~~
289 ~~flux, regardless of the uncertainty in fluxes associated with spatial averaging.~~

290 **2.4 Evaluation scheme**

291 **2.4.1 Wind measurement evaluation**

292 The key to successful aircraft EC measurements lies in the translation of accurately measured, aircraft-orientated, wind vector
293 to geo-referenced orthogonal wind vector (Thomas et al., 2012). Determining the geo-referenced wind vector requires a
294 sequence of thermodynamic and trigonometric equations (Metzger et al., 2012), these equations propagate various sources of
295 error to the measured geo-referenced wind vector. To estimate the measurement errors in the geo-referenced wind vector, we
296 used the linearized Taylor series expansions of Eqs. (S15) to (S17) derived by Enriquez and Friehe (1995) (Eqs. S18 to S20 in
297 Supplement Part A) to determine the sensitivities of each of the geo-referenced wind vector components with respect to the
298 relevant variables. Then, these sensitivity terms can be combined to compute the overall measurement error (1σ) in the geo-
299 referenced 3D wind vector (Eqs. S21 to S23 in Supplement Part A).

300 The above wind measurement error analysis gives the nominal measurement precision of the geo-referenced wind, but does
301 not consider the influence of environmental changes. Following the methods of Lenschow and Sun (2007), we assess whether
302 the accuracy of wind measurements from the UAV in satisfying the minimum signal level needed for resolving the mesoscale
303 variations of the three wind components in the encountered atmospheric conditions. Firstly, the minimum required signal level
304 for measurement of vertical air speed (ω) under the encountered atmospheric conditions could be estimated as (Lenschow and
305 Sun, 2007):

306 $$\frac{\partial w}{\partial t} < 0.2\sqrt{2}\overline{\sigma_w}2\pi k U_a \tag{1}$$

307 with the true airspeed (U_a) set to mean cruise speed 30 m s^{-1}, σ_w is the peak signal magnitude ~~(σ_w)~~ of the power spectra, and
308 k is the corresponding wavenumber ~~(k)~~ (Thomas et al., 2012). The measurement error ~~of the system~~ in the vertical wind
309 component can be calculated as (Lenschow and Sun, 2007):

310 $$\frac{\partial w}{\partial t} \cong \Theta \frac{\partial U_a}{\partial t} + U_a \frac{\partial \theta}{\partial t} + \frac{\partial w_{UAV}}{\partial t} \tag{2}$$

311 with $\Theta = \alpha - \theta$, where α is the attack angle, θ is the pitch angle, w_{UAV} is the UAV's vertical velocity. According to Lenschow

312 and Sun (2007), the signal level and mesoscale fluctuation of horizontal wind components (u and v) are considerably larger

313 than that of vertical wind, so the accuracy criteria are not nearly as stringent. The measurement error of the horizontal wind

314 component could be calculated as (Lenschow and Sun, 2007):

315 $$\frac{\partial u}{\partial t} \cong -\frac{\partial U_a}{\partial t} + \frac{\partial u_{UAV}}{\partial t} \qquad\qquad (3)$$

316 $$\frac{\partial v}{\partial t} \cong \Psi \frac{\partial U_a}{\partial t} + v_{tas} \frac{\partial \Psi}{\partial t} + \frac{\partial v_{UAV}}{\partial t} \qquad\qquad (4)$$

317 and,

318 $$\Psi \equiv \psi' + \beta \qquad\qquad (5)$$

319 where u_{UAV}, v_{UAV} are the UAV's horizontal velocity measured from INS, ψ' is the departure of the measured true heading

320 from the average true heading, and β is the sideslip angle of airflow. If the measurement error of the 3D wind vector from Eqs.

321 (2) to (4) is smaller than the required minimum signal level of the vertical and horizontal wind components, it can be confirmed

322 that the measurement accuracy of the geo-referenced 3D wind vector from UAV is sufficient to resolve the mesoscale

323 variations of the three wind components in the encountered atmospheric conditions.

324   In addition, accurate measurements of geo-referenced wind vector typically not only depend on the measurement precision

325 of the sensors (i.e., 5HP and INS), but also related to the quality of the calibration parameters and the geometry structure of

326 the UAV ~~EC system~~ (i.e., flow distortion and leverage effect). For evaluation of the effect of the latter two ~~aspects~~, a calibration

327 flight campaign (Section 2.2.1) was performed to determine the calibration parameter (ϵ_ψ, ϵ_θ), check its quality, as well as to

328 ascertain the effects of the lever arm and up-wash by the wings. The methods for acquiring the calibration parameter were

329 given by Vellinga et al. (2013) and Sun et al. (2021a), and the results are reported in Supplement Part C (Figs. S2 and S3).

330 During the in-flight calibration campaign, a 'racetrack' maneuver was performed to check the quality of the calibration

331 parameters determined from the 'box' flight maneuver. The initial ($\epsilon_\psi = 0°$, $\epsilon_\theta = 0°$) and calibrated ($\epsilon_\theta = -0.183°$, $\epsilon_\psi = 2°$,

332 in Supplement Part C) set of parameters were used to calculate the geo-referenced wind vector. By comparing the mean and

333 standard deviation of the horizontal and vertical wind vector between the initial and calibrated set, the quality of the geo-

334 referenced wind vector measurement in real environment conditions can be verified.

335   The relative wind vector ($\hat{U}_a$) measured by the aircraft is susceptible to flow distortion because the airplane must distort the

336 flow to generate lift and thrust~~., and T~~the aircraft's propellers, fuselage, and wings are the main sources of flow distortion as

337 flow barriers (Metzger et al., 2011). For fixed-wing aircrafts, the wind probe mounted on the nose of the UAV and extended

338 as far forward of the fuselage as possible could avoid ~~significant influence from~~the flow distortion ~~from~~ induced by the fuselage

339 and propellers. ~~Nevertheless, e~~Effects from the induced upwash by the wings can also ~~significantly~~ influence the

340 correspondence between the measured and free-stream flow variables (Garman et al., 2008). The induced upwash ~~by the wings~~

341 modifies the local angle of attack, causing the measured attack angle (α) to be larger than the free-stream attack angle (α_∞)~~.~~

342 ~~The magnitude of upwash influence generally increases with airplane size and airspeed, typically ranging from 0.5 to 2.5 m s⁻~~
343 ~~¹ as reported by the manned fixed-wing aircraft~~ (Garman et al., 2008). Therefore, for wind measurements by large-scale
344 manned fixed-wing aircrafts, the upwash effects must be corrected (Garman et al., 2008; Kalogiros and Wang, 2002). However,
345 ~~wind measurements using a multi-hole probe on the~~ UAV seldom need this correction due to the fuselage size and ~~because~~ the
346 airspeed is very low compared to a manned aircraft.

347 In this study, I~~i~~n order to access whether the lift-induced upwash could be safety ignored by the current UAV-based EC
348 system, an~~the~~ 'acceleration-deceleration' flight maneuver was performed. According to Crawford et al. (1996), the pitch angle
349 (θ) by the INS instrument can be utilized as an estimate of the free-stream attack angle (α_∞) if the aircraft's vertical velocity
350 is zero, since it is unaffected by lift-induced upwash and varies directly with α_∞ when the ambient vertical wind is zero. Under
351 ideal conditions (zero aircraft vertical velocity and zero ambient vertical wind), the approximation relationship of $\theta \cong \alpha_\infty$ is
352 valid when $\theta < 6°$ (Crawford et al., 1996; Vellinga et al., 2013). Departures from the 1:1 relationship can be caused by airflow
353 distortion around the airplane behind the 5HP. The 'acceleration-deceleration' maneuver produced various pitch and attack
354 angles measured under various airspeeds, which allowed a direct comparison between the pitch angle (θ) and the attack angle
355 (α). If the slope between α and θ is close to unity, it indicates that the influence of lift-induced upwash can be ignored;
356 otherwise, its influence should be corrected ~~using upwash models~~ (Garman et al., 2006). Meanwhile, the influence of leverage
357 effects was also evaluated based on the measurement data from the 'acceleration-deceleration' maneuver by considering or
358 ignoring the leverage effect correction term in Eqs. (S15) to (S17).

359 2.4.2 Flux measurement error caused by instrumental noise

360 ~~Errors or uncertainties in EC measurements can be systematic or random.~~ Flux M~~m~~easurement error from UAV~~, they~~ can be
361 attributed to several sources, mainly including instrumental noise, data handing, atmospheric conditions, ~~insufficient flux~~
362 ~~calculation~~spatial averaging length, and bumpy flight environment (Mahrt, 1998; Finkelstein and Sims, 2001; Mauder et al.,
363 2013). They can be systematic or random. ~~Knowledge of the measurement precision is of great importance for interpretation~~
364 ~~of EC measurements especially when detecting small fluxes in terms of turbulent exchange or signal-to-noise (SNR) of the~~
365 ~~instrumentation.~~ Determination of the flux measurement error ~~from~~ caused by instrument noise is very useful, as it is related
366 not only to the system performance, but also to the minimum resolvable capability for the flux to be measured. In the current
367 study, uncertainty related to instrumental noise (listed in Table 1) was estimated ~~with a~~using the directly method proposed by
368 Billesbach (2011). This method can be called as "random shuffle" (denoted as the RS) method and was "designed to only be
369 sensitive to random instrument noise". According to Billesbach (2011), the uncertainty of the flux covariance can be expressed
370 as:

371 $$\sigma_{\overline{w'x'}} = \frac{1}{N}\sum_{i,j=1}^{N} w'(t_i)x'(t_j) \qquad\qquad\qquad (6)$$

372 where x is the target entity of the covariance, N is the number of measurements contained in the block averaging period, $j \in$
373 $[1 \dots N]$ but the values are in the random order. The idea behind the RS method was that the randomly shuffled will remove

374 the covariance between biophysical (source/sink) and transport mechanisms, leaving only the random "accidental" correlations

375 attributed mostly to instrument noise (Billesbach, 2011). It means that the shuffled component x makes it uncorrelated in

376 time/space and decorrelates x from w, resulting in two independent variables (i.e., $\overline{w'x'}\sim0$), and any residual value (i.e.,

377 $\overline{w'x'} \neq 0$) of the covariance is attributed to random instrument noise. ~~In addition to the basic assumptions made in EC flux~~

378 ~~calculation, one additional assumption in RS method is that the block averaging period should be sufficiently long to accurately~~

379 ~~represent the lowest significant frequencies contributing to the covariance which could be verified by forming Ogive plots of~~

380 ~~the covariance (Billesbach, 2011).~~

381 In this study, in order to obtain a robust estimate~~s~~ of the instrumental noise, $\sigma_{\overline{w'x'}}$ was repeatedly calculated 20 times for

382 every straight and level flight leg in operation flight (Fig. 2), and the mean of the absolute values of these ~~20 replicated~~repeated

383 estimate~~s~~d ~~for~~ $\sigma_{\overline{w'x'}}$ were used to estimate the random uncertainty related to instrumental noise. According to Rannik et al.

384 (2016), RS method tends to overestimate the covariance uncertainty ~~due to instrumental noise only~~. Then, the uncertainty in

385 the flux covariance of sensible heat ($\sigma_{\overline{w'T'}}$), latent heat ($\sigma_{\overline{w'\rho_v'}}$), and CO_2 ($\sigma_{\overline{w'\rho_c'}}$) were estimated using RS method, respectively.

386 It should be noted that the measurement error of EC flux ~~measurement~~ is influenced not only by the uncertainty in the raw

387 covariance but also by the propagated errors form the correction terms (i.e., WPL correction) or any lens contamination

388 (Serrano-Ortiz et al., 2008). ~~For EC measurement from our UAV, t~~The signal quality of the IRGA wa~~s~~is checked before each

389 flight measurement to ensure that the measurement of gas concentration is not affected by lens contamination. The ~~final~~ relative

390 uncertainty of flux measurement was ~~evaluated~~estimated using the partial derivatives of the ~~full~~ flux calculation equation ~~with~~

391 ~~respect to their flux value~~ derived by Liu et al. (2006) (Eqs. ~~S29~~S28 to ~~S31~~S30 in Supplement Part B). These equations ~~(Eqs.~~

392 ~~S29 to S31)~~ ignored the perturbations terms from the errors in the individual scalar (i.e., ρ_v, ρ_c, T) which were proved

393 ~~negligible~~ very small (Serrano-Ortiz et al., 2008). At last, after several repetitive calculation of the Eq. (6), their averaged value

394 then be combined to Eqs. (~~S29~~S28) to (~~S31~~S30) for estimating the ~~final~~ flux measurement error ~~due to~~caused by instrumental

395 noise.

396 **2.4.3 Resonance effects**

397 Previous work found that the measurement of the atmospheric scalars (e.g., air temperature, H_2O, and CO_2 concentration) by

398 the current UAV-based EC system ~~is~~were susceptible to resonance effects caused by the operation of the engine and propeller

399 (Sun et al., 2021b). In order to further reduce the noise influence from resonance effects, the vibration damping structure ~~of~~

400 ~~the developed UAV-based EC system~~ was further optimized. ~~Then, T~~the ~~reference~~reference (co)spectra curve of Massman

401 and Clement (2005) was used to quantify the influence of the resonance effects remaining after vibration isolation optimization.

402 Massman and Clement (2005) gave the generalization mathematical expression of the models of spectra and co-spectra:

403 $$Co(f) = A_0 \frac{1/f_x}{[1+m(f/f_x)^{2\mu}]^{\frac{1}{2\mu}(\frac{m+1}{m})}} \tag{$\cancel{6}7$}$$

404 where f is frequency (Hz), f_x is the frequency at ~~which~~ where $fCo(f)$ reaches its maximum value, A_0 is a normalization

405 parameter, m is the (inertial subrange) slope parameter, and μ is the broadness parameter. To describe co-spectra, m should

406 be 3/4; to describe spectra, m should be 3/2. According to Massman and Clement (2005), ~~$\mu = 7/6$~~ was set to 7/6 under stable

407 atmospheric condition and ~~$\mu = 1/2$~~ was set to 1/2 under unstable atmospheric condition. Fast Fourier transform (FFT) method

408 was used to calculate the spectra and co-spectra of the measured turbulent variables. Before calculating the turbulence

409 (co)spectra, condition of the raw turbulence data was performed, including ~~a~~ linear detrend and tapering using the Hamming

410 window to reduce the spectral leakage (sharp edge) according to Kaimal et al. (1989).

411 ~~According to Sun et al. (2021b), t~~The noise influence from resonance mainly appears in the high frequency domain.

412 According to the feature of spectral curve, the frequency range of the noise region was artificially designated to $f > 8$ Hz for

413 air temperature, $f = 1\sim5$ Hz for water vapor, and $f = 1\sim8$ Hz for CO_2. The normalized spectra and co-spectra curve were

414 adopted and the area difference of the designated frequency range beneath the (co)spectra curve between the measured and

415 reference (co)spectra curve was calculated to quantify the influence of resonance noise in the variance and flux covariance of

416 the measurement atmosphere scalars. An example is shown in Figure 3, and also shown ~~is~~ the reference (co)spectra curve of

417 Massman and Clement (2005), with the (co)spectral maximum at $f_x = 0.1$. The red region in Fig. 3 represent~~ed~~s the impact

418 extent of the resonance noise in the variance (Figs. 3a to 3c) and flux covariance (Figs. 3d to 3f) of the measured scalars. ~~The~~

419 ~~systematic noise deviation in the fluxes of sensible, latent heat and CO₂ could be derived relative to the entire frequency range.~~

420

421
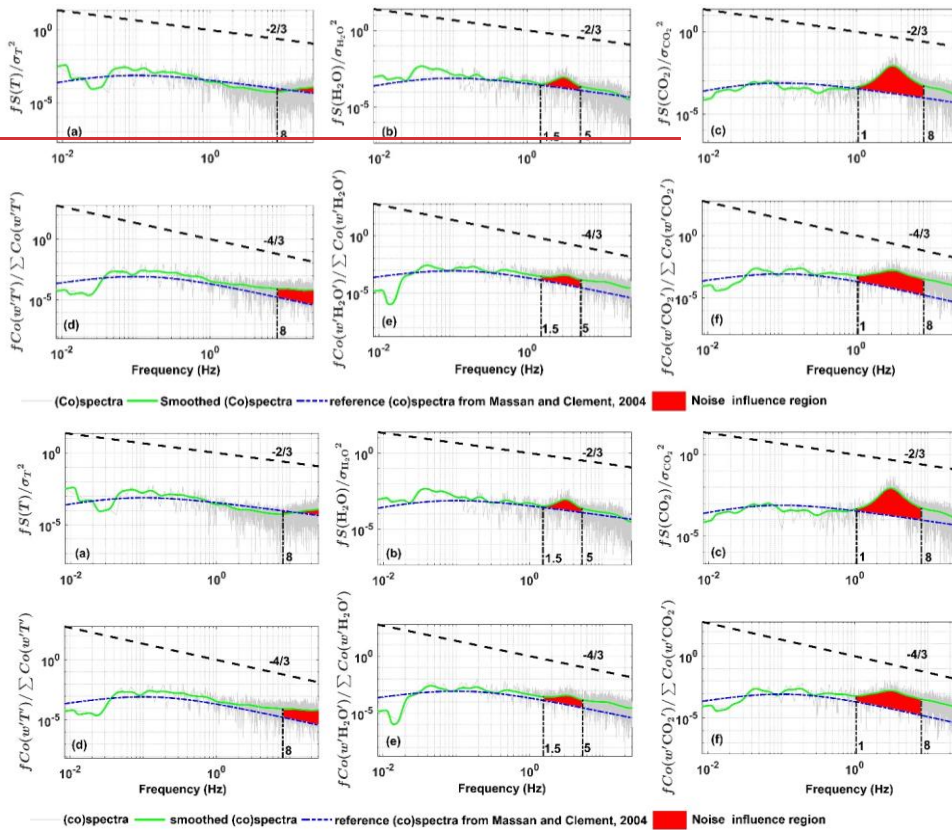
Figure 3. ~~The i~~Influence of ~~the~~ resonance noise on the spectra (top row) and co-spectra (bottom row) curve of the measured scalars based on the ~~measurement~~ measured data from ~~the~~ one standard operation flight ~~campaign~~ carried out on 8 August 2022 at Dagang district, Tianjin, China. The red region is the area difference of the designated frequency range (vertical black dashed-dotted line) beneath the (co)spectral curve between the measured and reference (co)spectral curve.

2.4.4 Sensitivity analysis

To understand the relevance of the calibration parameters for the measurement of geo-referenced wind vector and turbulent flux, two sensitivity tests were conducted. The magnitude of the perturbation in the wind vector and turbulent flux was investigated as a function of the uncertainties in the four calibration parameters, including three mounting misalignment angles

430 ($\epsilon_\psi, \epsilon_\theta, \epsilon_\phi$) between the 5HP and the CG of the UAV and one temperature recover factor ($\epsilon_r = 0.82$) used to calculate the

431 ambient temperature (Eq. 3 in Sun et al. 2021a).

432 First, the sensitivity of the geo-referenced ~~3D~~ wind vector and turbulent flux to the uncertainties ~~of~~in the individual

433 calibration parameter was investigated. The geo-referenced ~~3D~~ wind vector and turbulent flux ~~was~~ were calculated based on

434 the straight leg (about 4 km) of the standard operational flight by adding an error of ± 30 % to the ~~optimum~~ calibrated value

435 of each calibration parameter alternately; except for ϵ_ϕ, for which the typical range of $\pm 0.9°$ was taken for sensitivity analysis

436 (Vellinga et al., 2013).

437 Then, in order to test the overall interaction between the parameters, a second sensitivity test was performed to calculate the

438 geo-referenced ~~3D~~ wind vector and turbulent fluxes by adding ± 30 % error to all calibration parameters simultaneously.

439 Lastly, their relative errors (*RE*) with respect to the original value were calculated to evaluate the perturbation of the wind

440 vector and turbulent flux under the variation of each calibration parameter as well as under simultaneous variation of all

441 calibration parameters. ~~During~~ In the sensitivity analysis, the calculated geo-referenced wind and turbulent flux ~~results~~ whose

442 absolute value was less than their least resolvable magnitude were filtered out to avoid the influence of the errors contained in

443 the measurements themselves on the results.

444 **2.4.5 Relative error**

445 In this study, relative error (*RE*) was used to evaluate the influence of different factors on the measurements of geo-referenced

446 wind vector and turbulent flux ~~by the UAV-based EC system~~. It is defined as:

447 $RE = \frac{|x_0| - |x|}{|x|} \times 100$ %   (7)

448 where '| |' means the absolute value, x is the 'true' value, x_0 is the influenced value. *RE* > 0 means the exerted influence will

449 cause the measurement value to be larger than 'true' value and vice versa.

450 **3 Results**

451 **3.1 Wind measurement evaluation**

452 ~~Evaluation of the w~~Wind measurement ~~performance~~ evaluation ~~from~~for the UAV-based EC system includes three contents:

453 (1) measurement precision and its ability to resolve the mesoscale variations of the wind, (2) checking the quality of the

454 acquired calibration parameters, and (3) checking whether the measured wind vector is affected by upwash flow and leverage

455 effects.

456 First, according to the equations described in Supplement Part A (Eqs. S18 to S23), the measurement precision ~~for~~of

457 horizontal wind components is a function of true airspeed and true heading, while, the measurement precision ~~of~~for vertical

458 wind component is largely decided by the true airspeed. The typical values of true airspeed ranging from 25 m s^{-1} to 35 m s^{-1}

459 (interval of 1 m s^{-1}) and the true heading values ranging from 0° to 180° (interval of 30°) were used in the evaluation of wind

460 measurement error. Then, the measurement precision (1σ) of the geo-reference 3D wind vector from aircraft was estimated

461 using the measurement precision of the related parameters from Table 1. The results are shown in Figure 4 for the measurement

462 precision of horizontal wind (σ_u and σ_v in Figs. 4a and 4b) and vertical wind (σ_w in Fig 4c), respectively. The typical values

463 of the measurement precision are ranging from 0.05 m s^{-1} to 0.07 m s^{-1} for horizontal wind component u, ranging from 0.02 m

464 s^{-1} to 0.08 m s^{-1} for horizontal wind component v, and ranging from 0.05 m s^{-1} to 0.07 m s^{-1} for vertical wind component w.

465 ~~When the flight direction is towards due east or due west, the horizontal wind (u and v) has the smallest measurement error.~~

466
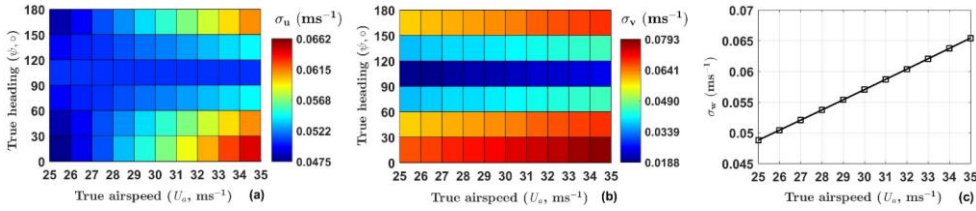
467 **Figure 4. Estimated measurement precision (1σ) of the horizontal wind (a, b) and vertical wind (c) according to the equations**
468 **described in Supplement Part A (Eqs. S18 to S23).**

469 Generally speaking, an autopiloted UAV can maintain a near-constant true airspeed during the cruise flight phase. ~~For~~ At a

470 true airspeed of 30 m s^{-1} for the current UAV ~~based EC system~~ during the cruising, the maximum measurement error in the

471 northward, eastward, and vertical velocities of the geo-referenced wind components were calculated as approximately 0.06,

472 0.07, and 0.06 m s^{-1}, respectively. Then, we assume that a minimum signal-to-noise ratio of 10:1 is required to measure the

473 wind components with sufficient precision for EC measurement~~s~~ (Metzger et al., 2012). Accordingly, in the real environments,

474 horizontal and vertical wind speed greater than 0.7 m s^{-1} and 0.6 m s^{-1} can be reliably measured, respectively (Table 2).

475 **Table 2**: The maximum measurement error in the northward (u), eastward (v), and vertical (w) velocities of the geo-referenced

476 wind components at the true airspeed of 30 m s^{-1}, and the least resolvable magnitude assuming the minimum required signal-

477 to-noise ratio of 10:1.

Measurements	Measurement precision (1σ)	Least resolvable magnitude
u-windspeed (m s^{-1})	0.06	0.6
v-windspeed (m s^{-1})	0.07	0.7
w-windspeed (m s^{-1})	0.06	0.6

478 The above results gave the nominal precision for wind measurement~~s~~ that does not consider the influence of environmental

479 conditions. Changes in the environment will lead to sensor drift, increasingly deteriorating the measurement with flight

480 duration (Metzger et al., 2012; Lenschow and Sun, 2007). Following the methods of Lenschow and Sun (2007), the ability of

481 ~~the limitations of the accuracy of~~ wind ~~field~~ measurements from UAV to resolve the mesoscale variations of the 3D wind

482 components in the encountered atmospheric conditions was assessed. For the vertical wind, the mesoscale variability was

483 defined as the peak signal magnitude of the power spectra curve. The corresponding average wavenumber was determined as

484 0.09 m^{-1} based on the straight flight leg (about 4 km, lasting about 120 s) of the standard operational flight. Then, according

485 to Eq. (1), the minimum required signal level for the vertical wind measurement was estimated as $\partial w/\partial t \simeq 0.14$ m s^{-2}. The

486 accuracy of the vertical wind measurement using Eq. (2) is estimated as follows. The first term on the right-hand side of Eq.

487 (2) is dominated by the drift in the differential pressure transducer, the value of $\partial U_a = 0.05$ m s^{-1} acquired from the wind

488 tunnel test was ~~applied~~ used (Table 1). The histogram of Θ derived from the standard operational flights is shown in Figure 5.

489 The 99 % confidence interval indicates that the value of Θ seldom exceeds ±3°, i.e., ±0.053 radians. Thus, the value of the

490 first term was estimated as 2.2×10^{-5} m s^{-2}.

491
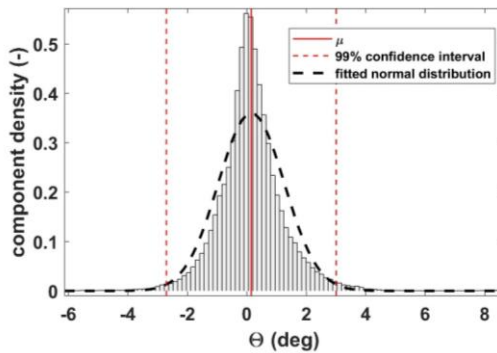
492 **Figure 5. Histogram of Θ derived from the standard operational flights. Component density is scaled so that the histogram has a**
493 **total area of one. Red vertical lines indicate distribution average (solid) and 99% confidence interval (dashed). The black dashed**
494 **bell curve displays a reference fitted normal distribution.**

495 The second term in Eq. (2) is a combination of INS pitch accuracy and ~~drift in the measured~~5HP attack angle~~s~~ accuracy.

496 The combined accurac~~iesy~~ of these two sensors were applied to derive $\partial\Theta = 0.0024$ radians. Thus, the second term in Eq. (2)

497 was estimated as 6×10^{-4} m s^{-2}. Finally, the third term in Eq. (2) was estimated as 1.7×10^{-4} m s^{-2}, according to the stated

498 accuracy of the vertical velocity from the INS. The overall performance of the vertical wind measurement (7.9×10^{-4} m s^{-2})

499 was accurate enough to resolve the mesoscale variations in vertical air velocity.

500 The required accuracy of horizontal wind for mesoscale measurement was estimated as 10 times larger than that of vertical

501 wind, i.e., $\partial u/\partial t \simeq \partial v/\partial t \simeq 1.4$ m s^{-2}. The measurement accuracy of the horizontal wind component u was estimated as

502 4.8×10^{-4} m s^{-2} according to Eq. (3). Like the first term in Eq. (2), with the value of Ψ rarely exceeding ±0.18 radians, the

503 measurement accuracy of the horizontal wind component v was estimated as 2.7×10^{-2} m s^{-2}according to Eq. (4). Thus, the

504 measurement accuracy of the horizontal wind components was accurate enough to resolve the mesoscale variations in the

505 horizontal air velocity as well.

506 Second, before checking the quality of the acquired calibration parameters, the calibration results of the offset in pitch (ϵ_θ)
507 and heading (ϵ_ψ) angles based on the 'box' maneuver are provided in Supplement Part C (Figs. S2 and S3). The final calibration
508 values are $\epsilon_\theta = -0.183°$ and $\epsilon_\psi = 2°$. In order to verify the quality of these calibration parameters, a 'racetrack' maneuver
509 was performed. Figure 6 shows the ~~verification~~ validation results by plotting wind vector and calculating summary statistics
510 for the 'racetrack' maneuver (including turns), using the initial ($\epsilon_\theta = \epsilon_\psi = 0°$, Fig. 6a) and calibrated (Fig. 6b) set of
511 parameters, respectively. ~~The i~~Introduction of the calibration parameter effectively improved the quality of geo-referenced
512 wind vector measurement. The standard deviation for wind direction, $\sigma_{U_{dir}}$, is 4.9° for the calibrated set compared to 8.7° for
513 the initial set, and the standard deviation of wind speed, σ_U, is 0.52 m s^{-1} for the calibrated set compared to 1.12 m s^{-1} for the
514 initial set. The averaged vertical wind speed is much closer to zero ($\bar{w} = -0.006$ m s^{-1}) for the calibrated set than for the
515 initial set ($\bar{w} = 0.1$ m s^{-1}). For the horizontal wind, it is evident from Fig. 6 that the measurement of wind direction and
516 velocity are little affected by sharp turns. On the contrary, the measurement of the vertical wind component is obviously
517 affected by turns in flight, as shown by the large ~~ripple~~ fluctuations in the vertical wind speed around the scan value of 150
518 (bottom panels in Fig. 6). It should be noted that the influence of upwash flow and the leverage effect are not considered in the
519 calculated ~~of~~ geo-referenced wind vector.
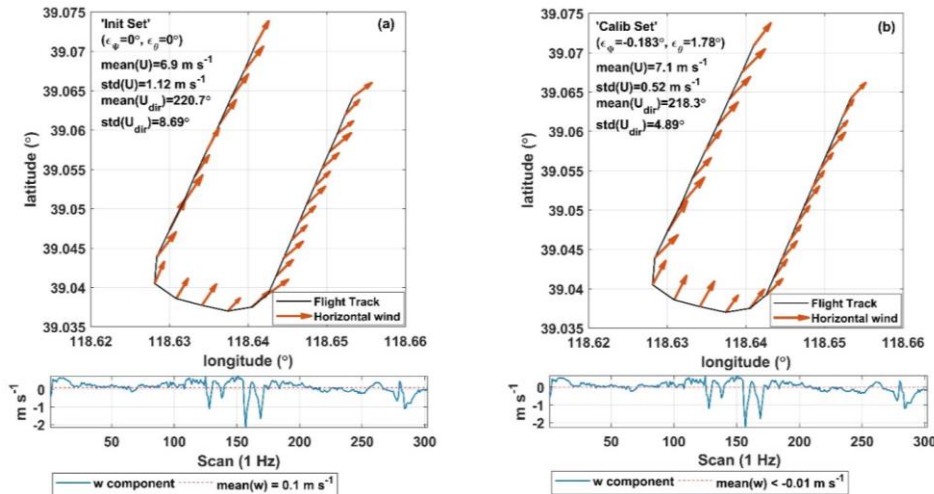
520

521 **Figure 6. Quality check of the calibration parameter by plotting wind vector and calculating summary statistics for the 'racetrack'**
522 **maneuver, using the initial (a) and calibrated (b) set of parameters, respectively. The calibration flight was carried out on 4**
523 **September 2022 at the Caofeidian Shoal Harbor in the Bohai Sea of northern China.**

524 Third, in order to check the influence of the lift-induced upwash on the measured attack angle ~~measurement~~ from the 5HP,
525 an 'acceleration-deceleration' flight maneuver was performed. During the 'acceleration-deceleration' maneuver, INS data

526 shown a vertical velocity of the UAV at 0.05±0.2 m s⁻¹, the altitude of UAV at 392±0.6 m, the heading of UAV at 199±2.4°.

527 We assumed that Tthe flight conditions meet the requirements of the 'acceleration-deceleration' maneuver (Vellinga et al.,

528 2013). The relationship between the pitch angle (θ) measured by the INS and the attack angle (α) measured by the 5HP is

529 plotted in Figure 7, where the attack angle was not corrected for lift-induced upwash. The slope (0.94) between θ and α is

530 close to its theoretical value of 1, and the intercept (0.16) is close to zero. This resultIt indicates that the lift-induced upwash

531 has only a very small effect on the attack angle, and the influence of upwash could be ignored.
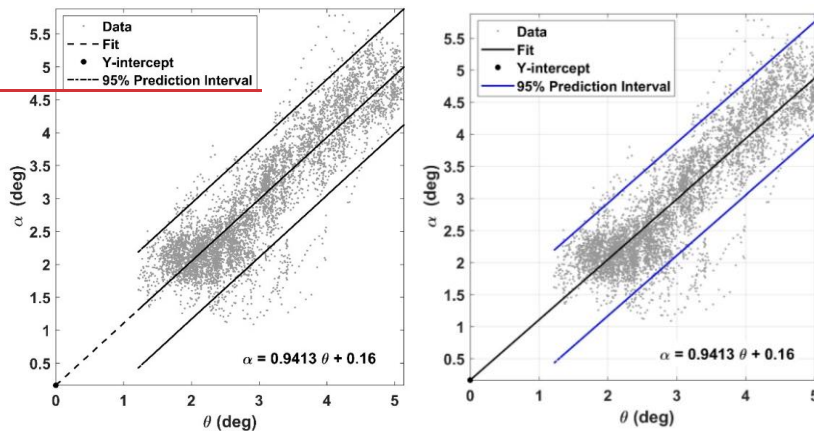
532

533 **Figure 7. Relationship between the pitch angle (θ) measured by the integrated navigation system (INS) and the attack angle (α)**
534 **measured by the 5HP5-hole probe (5HP). The fitted linear equation is also shown.**

535 Finally, the geo-referenced wind vector was calculated with and without the correction for the leverage effect based on the

536 measurement data from the 'acceleration-deceleration' flight maneuver. The averaged relative differences between the

537 corrected and uncorrected horizontal and vertical wind speeds are 0.1 % and 0.2 %, respectively. The standard deviation for

538 horizontal wind speed is 0.307 m s⁻¹ without the level arm term compared to 0.306 m s⁻¹ when the level arm term is introduced.

539 The standard deviation of vertical wind speed is 0.254 m s⁻¹ without the level arm term compared to 0.253 m s⁻¹ with the level

540 arm term. The correction of leverage effect had minimal effect on improving the geo-referenced wind vector measurement;

541 therefore, this correction term can be ignored.

542 **3.2 Flux measurement error caused by instrumental noise**

543 Flux measurement error caused by the instrumental noise gives the lowest limit of the flux value that the UAV-based EC

544 system is able to measure. Such measurement errorIt was assessed by combining the covariance uncertainty estimated by RS

545 method and the propagation of errors in flux correction terms. Before estimating the flux covariance uncertainty using RS

546 method, using the measured data from each straight and level flight leg of the standard operational flight (Fig. 2), the

547 normalized integrated cospectra (ogives) curves of sensible heat (Fig. 8a), latent heat (Fig. 8b), and CO_2 (Fig. 8c) flux are
548 formed as a function of wavenumber (k), where $k = 2\pi f / U_a$. As shown in Figure 8, although the heterogeneous turbulence
549 (or mesoscale turbulence) interfered the shape of ogive curves, most curves converged at the high and low frequency ends,
550 which indicated that these segmented data were sufficiently long to represent the lowest significant frequencies contributing
551 to the covariance (Sun et al., 2018).
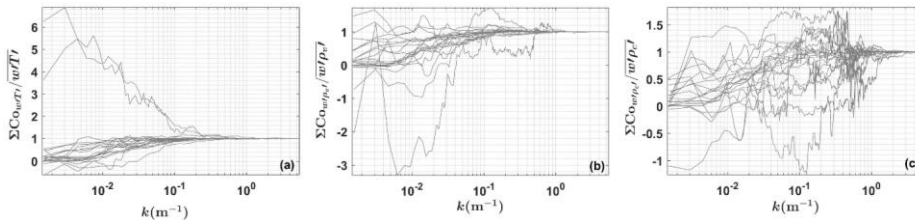
552
553 **Figure 8. Normalized ogive curves as a function of wavenumber for the flux covariance of sensible heat (a), latent heat (b), and CO_2**
554 **(c) from each straight and level flight leg of the standard operational flights in Section 2.2.2.**

555 ~~Then, t~~The results of instrumental noise related relative flux measurement error compared to the magnitude of the flux are
556 shown in Figure 9. It can be seen that the flux measurement error caused by instrumental noise significantly decreases when
557 the flux magnitude increases. It is not surprising since, in theory, instrumental noise is usually close to a constant and the
558 relative flux measurement error caused by instrumental noise will decreases with increasing measurement magnitude. Overall,
559 instrumental noise has the least effect on latent heat flux (ranging from 0.02% to 2.42% in this study) measurements, followed
560 by sensible heat flux (ranging from 0.05% to 8.6% in this study), and has the greatest effect on the measurement of CO_2 flux
561 (ranging from 0.22% to 75.6% in this study). Then, a simple rational function relationship between the relative measurement
562 error and the flux magnitude is fitted according to the measured data, where the constant term in the denominator is set to 0.
563 The fitted coefficient in the numerator can be considered as the flux measurement error caused by instrumental noises, which
564 are 0.03 μmol m^{-2} s^{-1}, 0.02 W m^{-2}, and 0.08 W m^{-2} for the measurement of CO_2 flux, sensible and latent heat flux, respectively.
565 At last, using the signal-to-noise ratio of 10:1, the minimum magnitudes for reliably resolving the CO_2 flux, sensible and latent
566 heat fluxes were estimated as 0.3 μmol m^{-2} s^{-1}, 0.2 W m^{-2}, and 0.8 W m^{-2}, respectively.
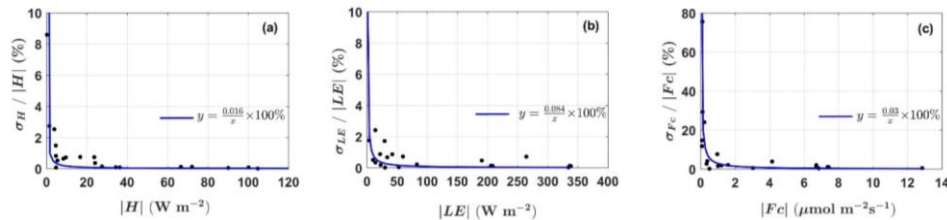
567
568 **Figure 9. Relative flux measurement error caused by the instrumental noise plotted against the magnitude of the flux. Also shown**
569 **the fitted error curves. Measured data was from the standard operation flights in Section 2.2.2.**

3.3 Resonance noise

The resonance noise from the engine and propeller can lead to systematic overestimation of the variance and covariance of the observed atmospheric scalars. ~~Since t~~The noise mainly appears in the high frequency domain of the (co)spectra, and the reference (co)spectral curve of Massman and Clement (2005) was used to quantify the systematically bias caused by the resonance noise.

All spectra curves of the variance of the measured scalars (including air temperature, H_2O, and CO_2 concentration) approximately followed the reference spectra curve and the reference -2/3 slope in the inertial subrange (Figs. 3a to 3c). The largest scatter occurred in the spectra of CO_2 (Fig. 3c). When comparing the spectra curve with the reference spectra, the resonance noise led to a systematic deviation in the variance of air temperature, H_2O, and CO_2 concentration of 0.1±0.1 %, 1.0±0.79 %, and 4.4±0.66 %, respectively~~, relative to the entire frequency range~~. For the flux covariance of sensible, latent heat and CO_2, all the co-spectra curves approximately follow the reference co-spectra curve and the reference -4/3 slope in the inertial subrange (Figs. 3d to 3f). Compared with the reference co-spectra, the resonance noise led to a systematic deviation in the flux of sensible, latent heat, and CO_2 of 0.07±0.004 %, 0.3±0.25 %, and 2.9±1.62 %, respectively~~, relative to the entire frequency range~~.

The results show that the resonance noise has a very little impact on the measured variance and flux covariance. ~~Among them, t~~The measurements of CO_2 concentration and flux are most susceptible to the resonance noise, but the impact of this noise is limited to around 5 % of the observed value.

3.4 Sensitivity analysis

~~In this study, i~~In order to investigate the relevance of the calibration parameters for the measurement of the geo-referenced wind vector and turbulent flux, two sensitivity tests were conducted by adding an error of ±30 % to the used ~~optimum~~ calibrated parameters ($\epsilon_\psi, \epsilon_\theta, \epsilon_\phi, \epsilon_r$). We assumed that the maximum uncertainties contained in the calibration parameter is not more than 30 % of its own value.

First, the sensitivity of the geo-referenced 3D wind and turbulent flux to the uncertainty in the individual calibration parameter was tested. The *RE* value is used to quantify the sensitivity, and the results are summarized in Tables 3 and 4. For the measurement of the geo-referenced wind vector, Table 3 shows that the uncertainties in the temperature recovery factor (ε_r) and 5HP mounting misalignment error in the roll (ϵ_ϕ) angle do not contribute significantly to errors in the wind measurements, which were typically smaller than 4% of the observed value in this study. Parameter ε_θ had the largest effect on the vertical wind component (up to 30 %), whereas ε_ψ had the largest effect on the horizontal wind component. For the measurement of turbulent fluxes, Table 4 shows that the errors in ε_r and ϵ_ϕ does not significantly influence the flux measurements, typically small than 5% of the observed value in this study. ~~The u~~Uncertainties in calibration parameter ε_θ and ε_ψ had significant effects on the measurement of turbulent flux~~es~~. ~~Adding an e~~Errors ~~of ±30 % to~~in ε_θ result in significant

601 perturbation (large *RE* variance) in the measured turbulent fluxes including sensible heat, latent heat and CO_2. While, errors

602 in ε_ψ to some extent mainly affect the measurement of latent heat flux (*RE* may up to 15 %).

603 **Table 3**: *RE* ~~from~~of the sensitivity test for the geo-referenced 3D wind vector (u, v, w). An error factor of ±30 % was added

604 to each calibrated parameter. The geo-referenced 3D wind vector was calculated based on the straight leg of the standard

605 operational flight.

Parameter	Error (%)	RE of geo-referenced 3D wind vector mean ± std		
		u (%)	v (%)	w (%)
ε_r	-30	0.04±0.41	-0.004±2	0±0
	30	0.06±0.43	0.27±1.1	-0.07±0.23
ε_φ *	-30	0.41±2.51	-0.09±2.05	1.15±2.43
	30	-0.43±2.61	0.09±1.79	-1.1±2.66
ε_θ	-30	0.03±0.41	-0.35±2.54	-30.51±6.42
	30	0.05±0.45	0.42±1.82	30.37±6.61
ε_ψ	-30	2.98±25.06	-2.04±16.3	0±0
	30	-2.97±24.96	2.42±16.63	0±0

606 * The optimum calibration value is set to 0, ε_φ was varied over $\pm0.9°$, which is 30 % of its typical range.

607 **Table 4**: *RE* ~~from~~of the sensitivity test for the turbulent fluxes. An error factor of ±30 % was added to each calibrated

608 parameter. The turbulent fluxes were calculated based on the straight leg of the standard operational flight.

Parameter	Error (%)	RE of turbulent flux mean ± std			
		Fc (%)	H (%)	LE (%)	u* (%)
ε_r	-30	1.04±3.04	-0.76±4.82	0.1±0.29	0±0
	30	-1.0±3.3	0.74±4.8	-0.1±0.29	0.2±1.07
ε_φ *	-30	0.07±1.2	0.03±0.7	0.15±1.51	0.54±1.71
	30	-0.14±0.89	-0.06±0.7	-0.16±1.46	0.12±1.61
ε_θ	-30	-3.27±11.18	-0.8±9.48	0.19±11.91	-4.08±5.61
	30	2.34±10.52	-0.44±8.24	-1.27±9.92	3.73±4.53
ε_ψ	-30	1.78±5.18	-0.73±4.87	1.89±13.42	0.63±5.75
	30	-0.99±3.96	-0.57±3.26	2.66±11.76	-0.59±4.42

609 * See Table 3.

610   The second sensitivity test was performed to evaluate the overall interaction between calibration parameters and the

611 calculation of geo-referenced wind vector and turbulent flux by adding an error of ±30 % to all the calibration members

612 simultaneously. Tables 5 and 6 provided a summary of the *RE* ~~results~~ from the second sensitivity test. For the measurement of

613 geo-referenced wind vector (Table 5), adding an error of ±30 % to all the calibration parameters at the same time resulted in

614 great perturbations to both the horizontal (low *RE* with high variance) and vertical wind components (high *RE* with low

615 variance). For the measurement of turbulent fluxes, adding 30% error in all of the calibration parameters can result in errors

616 in the measured fluxes more than 10%. In addition, Table 6 also reveals that the latent heat flux is more sensitivity to the errors

617 in the calibration parameter than other measured fluxes ~~measurement~~ (higher mean and variance of the *RE* compared to other
618 measurements).

619 **Table 5**: *RE* from~~of~~ the sensitivity test for the geo-referenced 3D wind vector (u, v, w) calculated by adding an error of ± 30 %
620 to all the calibrated parameter simultaneously. The geo-referenced 3D wind vector was calculated based on the straight leg of
621 the standard operational flight.

Parameter	Error (%)	*RE* of geo-referenced 3D wind vector mean ± std		
		u (%)	*v* (%)	*w* (%)
All	-30	4.24±27.89	-3.2±21.1	-29.35±4.63
	30	-4.15±27.46	3.55±21.91	29.16±4.86

622 **Table 6**: *RE* from~~of~~ the sensitivity test for the turbulent flux calculated by adding an error of ± 30 % to all the calibrated
623 parameter simultaneously. The turbulent flux was calculated based on the straight flight leg of the standard operational flight.

Parameter	Error (%)	*RE* of turbulent flux mean ± std			
		Fc (%)	*H* (%)	LE (%)	u* (%)
All	-30	-1.19±10.51	-0.9±8.06	2.71±13.91	-2.92±8.19
	30	-0.49±10.01	-1.66±5.4	-6.07±13.24	1.74±6.55

624 **4 Discussions**

625 ~~As one in a new generation of airborne flux measurement platforms, the UAV-based EC system can significantly reduce the~~
626 ~~cost of implementing airborne flux measurement campaigns and greatly promote their wide application at regional scales.~~ The
627 current study aimed to evaluate the ~~basic~~ performance of the UAV-based EC system developed by Sun et al. (2021a) in the
628 measurement of wind vector and turbulent flux.

629 First, the wind measurement precision (nominal precision) of the UAV-based EC system was estimated by propagating the
630 sensor errors to the geo-referenced wind vector using the linearized Taylor series expansions from Enriquez and Friehe (1995) .
631 The 1σ precision for~~of~~ geo-referenced wind measurement was estimated to be ± 0.07 m s^{-1}, and the least resolvable magnitude
632 for wind measurement was estimated at 0.7 m s^{-1} by assuming the minimum signal-to-noise ratio of 10:1. The derived wind
633 measurement minimum resolvable magnitude can be used as a basic reference for wind measurement capability of the UAV-
634 based EC system, and the measured values of wind vector smaller than the minimum resolvable values should be considered
635 unreliable. The accuracy of the sensors was also assessed by examining the collected data in the real environment ~~(Lenschow~~
636 ~~and Sun, 2007; Thomas et al., 2012)~~. Our results revealed that the overall performance of geo-referenced wind measurement
637 is sufficient accuracy for resolving the mesoscale variations of the 3D wind components under the encountered atmospheric
638 conditions. Therefore, it is possible to capture the mesoscale variability of the atmospheric boundary layer (ABL) over a wide
639 range of spatial scales by performing long~~er~~ flight paths.

640   Second, based on the measurement data from the in-flight calibration campaign, several key factors affecting the accuracy

641 of geo-referenced wind measurement were analysed. ~~First, t~~The UAV-based EC system was calibrated (in Supplement Part C)

642 using measured data from the 'box' flight maneuver to correct the mounting misalignment between the 5HP and the CG of the

643 UAV in the heading ($\epsilon_\theta = -0.183°$) and pitch ($\epsilon_\psi = 2°$) angles. The quality of the acquired calibration parameters was

644 verified using the measured data from 'racetrack' flight maneuver, and the acquired calibration value effectively improved the

645 observed wind field with smaller variance compared with the wind calculated using their initial value. At the same time, the

646 measurement of the vertical wind component was significantly affected by the in-flight turn (maintaining about 20° roll).

647 Therefore, it is necessary to avoid using the measured data from the turn section for turbulent flux calculation. Compared to

648 other studies (Vellinga et al., 2013; Reineman et al., 2013), the relatively large variance in the horizontal wind and wind

649 direction after calibrated in this study may be caused by the nonstationary condition of the turbulence. This was caused by the

650 reason that the flight altitude of 400 m was not high enough to totally avoid interaction from the underlying surface.

651   The current calibration procedure did not include methods to determine the offset angle in roll (ε_φ) and the temperature

652 recovery factor (ε_r) because of the small vertical separation (27.3 cm) between the 5HP and the roll axis of the UAV and the

653 small Mach number (<0.1) during operational flight. The default ($\varepsilon_\varphi = 0°$) and empirical ($\varepsilon_r = 0.82$) value were adopted for

654 these two calibration parameters. The sensitivity analysis shown these two parameters have no large effect on the wind vector

655 and turbulent flux.

656   It should be noted that wind measurement~~s~~ from the airborne platform may be susceptible to flow distortion and rigid-body

657 rotation (leverage effects). Generally, the influence of these two factors were ignored by UAV platform ~~when calculating the~~

658 ~~geo-referenced wind vector~~. To confirm that these effects could be safely ignored, data from 'acceleration-deceleration' flight

659 maneuver was used to analyse the effects of lift-induced upwash and the leverage effect on the wind measurements. Our results

660 demonstrate~~d~~ that the upwash has almost no effect on the wind measurement, which was indicated by the near 1:1 relationship

661 (0.94 in Fig. 7) between the measured attack angles and pitch angle. The slight departures from the ideal 1:1 relationship may

662 have been caused by the nonstationary condition during the flight. For the influence ~~from~~ of the leverage effects, the differences

663 in 3D wind vector between corrected and uncorrected for the leverage effect is very small as well. ~~Thus, i~~Ignoring the influence

664 of the leverage effect has almost no effect on the measurement of wind. Therefore, we concluded that the geo-referenced 3D

665 wind vector can be measured reliably by the current UAV-based EC system without considering the interference from the lift-

666 induced upwash and leverage effects.

667   Third, instrumental noise related ~~relative~~ flux measurement error was estimated by combining the covariance uncertainty

668 estimated by RS method and the propagation of errors in flux correction terms. By assuming that the instrumental noise ~~is~~ was

669 close to a constant, we fitted a simple rational function relationship between the relative measurement error and the flux

670 magnitude according to measured data (Fig. 9), and the fitted coefficient in the numerator can be considered as the flux

671 measurement error caused by instrumental noises. The estimated instrumental noise related flux measurement error of CO_2,

672 sensible and latent heat flux ~~are~~ were 0.03 μmol m^{-2} s^{-1}, 0.02 W m^{-2}, and 0.08 W m^{-2}, respectively. Since the RS method directly

uses the shuffled raw measurement data to calculate the instrumental noise in the flux covariance, ~~induced flux measurement error,~~ its estimate~~d result~~s inevitably included the effects of resonance noise from the UAV. Using the signal-to-noise ratio of 10:1, the least resolvable magnitude for turbulent flux measurement was estimated to be 0.3 µmol m^{-2} s^{-1} for the CO_2 flux, 0.2 W m^{-2} for the sensible heat flux, 0.8 W m^{-2} for the latent heat flux, respectively.

Fourth, because that the UAV-based EC system has not completely insulated the noise from the operation of the engine and propeller and its effect on the measured scalars, the reference (co)spectra of Massman and Clement (2005) was used to quantify the effect of the resonance noise on the variance and flux covariance of the measured scalars. ~~Previous studies found that t~~Due to the influence of resonance noise mainly ~~appears~~ appeared in the high frequency domain ~~of the power spectra of the measured atmospheric scalars (e.g., air temperature, H₂O, and CO₂ concentration).,~~ The frequency range of the noise region was we artificially designated the frequency range of noise region for air temperature, water vapor and CO_2 (Section 2.4.3). By calculating the area difference ~~of the designated frequency range beneath the (co)spectral curve~~ between the measured and reference (co)spectral curves for the designated frequency range, the resonance effect could be quantified. The results shown that, overall, resonance noise has little impact on the variance and flux covariance of the measured scalars. The measurements of CO_2 concentration and its flux covariance were the most susceptible to resonance noise, but the maximum effect was less than 5 %. It should be noted that this method may overestimate the deviation caused by the resonance noise ~~as indicated by~~due to the reference (co)spectra curve and the measured (co)spectra not fully overlapping in the inertial subrange (shown in Fig. 3).

~~In general, gas detection based on optical absorption methods can achieve fast and high precision gas concentration measurements, but they are extremely sensitive to vibration noise. However, due to the limited space inside the UAV, it is difficult to install all the hardware needed for a complex vibration isolation structure to effectively isolate the impact of vibration on the gas analyser. The weight and the aerodynamic shape of the UAV also present challenges. In the future, a new UAV-based EC system based on a pure electric UAV will be developed. The electro-powered UAV has similar performance to the current fuel-powered UAV but can minimize the impact of vibration noise from the engine and propeller rotation, which makes it possible to completely isolate the resonance effect using a simple vibration isolation structure. Electro-powered UAVs also have other advantages including larger wingspan (lower cruising speed), a constant CG position, and lower operational complexity compared to the current system.~~

Fifth, two sensitivity tests were conducted to assess the perturbation of the geo-referenced wind velocity and turbulent flux under variation (±30 %) of each calibration parameter around its ~~optimum~~ calibrated value ($\epsilon_\psi = 2°, \epsilon_\theta = -0.183°, \epsilon_\phi = 0°, \epsilon_r = 0.82$) as well as under simultaneous variation (±30 %) of all calibration parameters. Their RE was used to evaluate the sensitivity, and values of wind and flux less than their least resolvable magnitude were removed from the ~~calculation~~is analysis. The results revealed that uncertainties in the temperature recovery factor (ε_r) and mounting offset in roll angle (ε_φ) do not significantly contribute to an error in the measurement of wind vector ($RE < 4\%$) and turbulent fluxes ($RE < 5\%$). ~~The typical RE for the geo-referenced wind measurements is less than 1.2 % with variance less than 3 %, and the typical RE for turbulent flux is less than 1.1 % with variance less than 5 %.~~ Calibration parameters that had the largest effect on the

707 measurement of geo-referenced wind vector and turbulent flux are the mounting offset angle in pitch (ε_θ) and heading (ε_ψ).

708 Uncertainties in ε_θ had a direct effect on the measurement of vertical wind component, and then these errors propagate to the

709 measured fluxes, resulting in a large error ~~contains~~ contained in the measured fluxes (~15 %). A negative error in ε_θ will lead

710 to an underestimation of the vertical wind and vice versa. Errors in ε_ψ directly affect the measurement of the horizontal wind,

711 and to some extent, the measurement of turbulent flux. ~~The difference is that the added error in ε_ψ lead to a great variability~~

712 ~~(up to 25 %) in the *RE* of horizontal wind.~~ By checking the relationship between the magnitude of the horizontal wind (u, v)

713 and *RE*, a near ~~exponential~~ rational function relationship~~s~~ was seen, as shown in Figure 10. The influence of the error in the

714 ε_ψ decreased significantly with the increase in the magnitude of the horizontal wind velocity. Additionally, the measurement

715 of latent heat flux may be greatly affected by the error in ε_ψ, which is reflected by the relatively large deviancy (~14 %) of

716 the *RE*. Therefore, ~~calibration~~ the parameter ε_θ and ε_ψ need to be carefully calibrated.
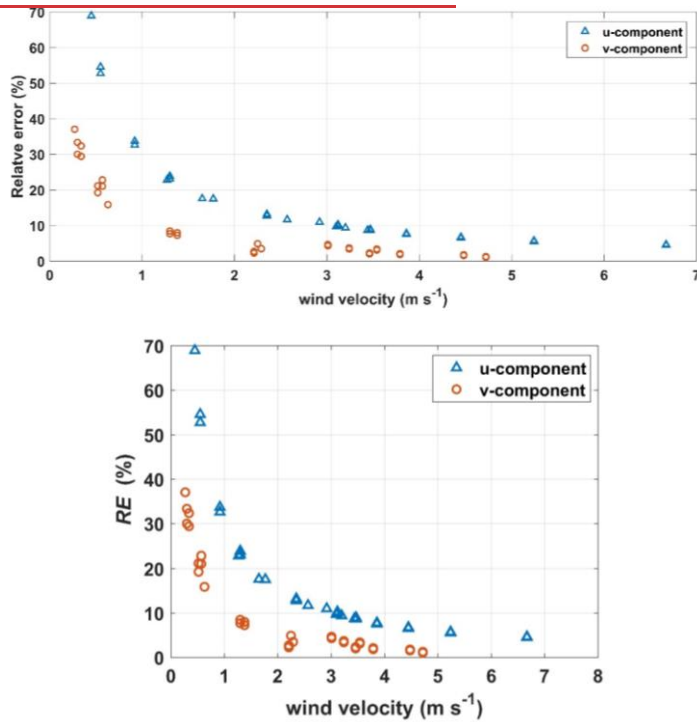
717

718

719 **Figure 10. Relationship between the magnitude of the horizontal wind velocity (u, v) and the relative error (*RE*) from the sensitivity**

720 **test.**

设置了格式: 字体: 非倾斜

721 Lastly, it should be noted that the accuracy of the measured geo-referenced wind ~~vector~~ field and turbulent flux from the

722 UAV-based EC system is subject to the combination of many factors, mainly including sensor accuracy, UAV powerplant,

723 UAV fluctuation (e.g., variation of the UAV attitude and flight height), and the atmospheric conditions during the

724 measurements, etc. This study mainly focused on assessing the effects of sensor precision and UAV powerplant on the

725 measurement errors of geo-referenced wind vector and turbulent flux. Evaluation results gave the lowest limit of the wind

726 ~~vector~~ field and turbulent flux that the UAV-based EC system can measure reliably. ~~Another effective way to evaluate the~~

727 ~~measurement accuracy of this new technique is by comparing measured values with those from the traditionally recognized~~

728 ~~measurement. However, tD~~he ~~d~~irect comparison of flux measurements between aircraft and traditional ground tower is still

729 challenging due to the difference in the measurement height, mechanism (time series for ground EC and space series for

730 aircraft), and instruments (e.g., wind sensor). Previous studies have extensively compared the measurement of fluxes and wind

731 vector between airborne and ground-based EC methods and found consistent results (Gioli et al., 2004; Metzger et al., 2012;

732 Sun et al., 2021b). At the same time, substantial and consistent over- or under- estimation of the measured wind and fluxes by

733 ~~UAV~~ aircraft compared to ground measurements were observed and reported. These differences may be due to several factors

734 such as vertical flux divergence (the measurement height of UAV is higher than ground-tower), surface heterogeneity (induced

735 by the larger footprint region of the UAV compared to the ground tower), measurement errors (e.g., window length, resonance

736 noise, etc.) as well as their difference in platform and sensors. Therefore, in order to evaluate the measurement performance

737 of the UAV-based EC system realistically, it is necessary to conduct a comparison test on the same platform and under the

738 same environment to exclude the influence of these factors. ~~Inspired by Reineman et al. (2013), future work can include~~

739 ~~developing a ground vehicle based UAV flux validation platform. This platform could carry both the UAV-based and~~

740 ~~traditional ground EC system to assess the measurement accuracy of the UAV-based EC system with the measurement of~~

741 ~~ground EC as the benchmark in a flight-like scenario.~~

742 **5 Conclusions and further works**

743 The main objective of this study was to quantitatively evaluate the performance of the developed UAV-based EC system in

744 the measurement of geo-referenced wind ~~vector~~ field and turbulent flux. In terms of measuring precision, ~~turbulence~~

745 ~~measurements from the UAV-based EC system were achieved with sufficient precision to enable reliable measurement of geo-~~

746 ~~referenced wind and EC flux. Magnitudes~~ magnitudes larger than 0.7 m s^{-1} for wind velocity, 0.3 µmol m^{-2} s^{-1} for CO_2 flux,

747 0.2 W m^{-2} for sensible heat flux, and 0.8 W m^{-2} for latent heat flux could be reliably measured by the UAV-based EC system

748 ~~by assuming the minimum required signal-to-noise ratio of 10:1 for EC application. Based on the data from the calibration~~

749 ~~flight, the cC~~arefully calibrated offset angle in pitch (ϵ_θ) and heading (ϵ_ψ) were shown to effectively improve the quality of

750 wind field measurements, and the influences of flow distortion and the leverage effect on the wind measurement were minimal

751 and could be ignored. The influence of resonance noise was small on the measurement of air temperature and water vapor

752 (typically < 1 % for their variance and flux covariance), but relatively large on the measurement of CO_2 (around 5 % for
753 variance and flux covariance).

754   The relevance of the calibration parameters $(\varepsilon_r, \epsilon_\phi, \varepsilon_\psi, \varepsilon_\theta)$ for the measurement of the geo-referenced wind vector and
755 turbulent flux was also assessed based on two sensitivity tests. The measurements of the geo-referenced wind vector and
756 turbulent flux were insensitive to the errors in the ε_r and ϵ_ϕ. While ~~U~~uncertainties in the calibration parameter~~s~~ ε_θ and ε_ψ had
757 the strongest effects on the measurements. Because of ε_θ ~~directly~~ determining the magnitude of the vertical wind, its error will
758 directly lead to uncertainties in vertical wind measurement and then propagate the uncertainties to the measure~~dment of~~
759 turbulent flux. ~~The uncertainties~~Errors in ε_ψ have a direct effect on the measurement of horizontal wind, and to some extent,
760 the measurement of turbulent flux. Therefore, these two calibration parameters need to be carefully calibrated. Conducting the
761 UAV-based EC measurement when wind velocity is larger than ~~2~~3 m s^{-1} can led to more stable and reliable ($RE <$ ~~20~~10%)
762 results of the wind speed measurement compared to a relatively windless environmental.

763   Finally, we concluded that the developed UAV-based EC system measured the geo-referenced wind ~~vector~~ field and
764 turbulent flux with sufficient precision. The lift-induced upwash and leverage effect had almost no effect on the measurement
765 of geo-referenced wind vector. The resonance effect caused by the operation of engine and propeller mainly affected the
766 measurement of CO_2, and its effect on variance and flux covariance was around 5 %. The quality of calibration parameters ε_ψ
767 and ε_θ has a significant effect on the measurement~~s~~ of the geo-referenced wind vector and turbulent flux, which ~~underscoring~~
768 underscores the importance of careful calibration. The UAV-based EC system has several advantages over manned aircraft,
769 including less turbulence disturbance in wind measurement, lower measurement altitude (above the ground level), simpler
770 operation, and lower operating costs, etc. However, there are still some shortcomings need to be overcome, such as resonance
771 noise, how large the difference compared to the tower-based EC under the same conditions, and how to interpret the
772 instantaneous flux results for the flight scenario (e.g., influence from surface heterogeneity, flux divergence, etc.). ~~Although~~
773 ~~UAV-based EC measurements have many advantages over manned aircraft and tower-based EC measurements, airborne EC~~
774 ~~measurements themselves have some shortcomings, such as flux results hard to interpret (e.g., influence from surface~~
775 ~~heterogeneity, flux divergence, etc.), the measurements are restricted to short periods of time, and the interaction between the~~
776 ~~UAV and turbulence.~~ Future researches may include the development of a new ~~generation~~ UAV-based EC system with the
777 following improvements: 1) a new electro-powered UAV platform with the advantages of being quieter (low noise), having a
778 low cruising speed~~, and being easy to operate~~; 2) a ground-vehicle-based validation platform to enable direct comparative
779 evaluation of the UAV-based EC system with traditional ground EC methods under near-identical environmental conditions;
780 3) a graphics based real-time monitoring system to make it possible to change the flight pattern according to real-time data;
781 and 4) conducting a number of integrated field observation experiments that combining ~~ground~~tower-based EC networks,
782 OMS, and multi-source satellite RS to further prompt the development of theory and methodology for ~~scaling~~
783 ~~transformation~~airborne flux measurements. Ultimately, the versatility of the UAV-based EC system as a low cost and widely

applicable environmental research aircraft ~~facilitates~~ will further ~~improving~~ improve our understanding of the energy and matter cycling processes at the regional scales.

Author contributions. SY, GB and LX planned the field campaign; SY, LB, JJ, ZZ and JS carried out the field measurements. SY, LS and XZ analysed the data and wrote the manuscript draft. SB, and QZ reviewed and edited the manuscript.

Competing interests. The authors declare that they have no conflict of interest.

Acknowledgments. This work was supported jointly by the Fundamental Research Funds for the Central Public-interest Scientific Institution (Grant No. 2023YSKY-27), and the National Natural Science Foundation of China (Grant No. 42101477). We would like to thank F-EYE UAV Technology Co. Ltd. for building, maintaining, and operating the UAV in this study. We would like to thank Dr. Joseph Elliot at the University of Kansas for her assistance with English language and grammatical editing of the manuscript.

Data availability. Data for this research are not publicly available due to its proprietary nature currently. The UAV calibration flight data and the standard operation flight data in this study are available upon request to the corresponding author.

References

Anderson, K. and Gaston, K. J.: Lightweight unmanned aerial vehicles will revolutionize spatial ecology, Frontiers in Ecology and the Environment, 11, 138-146, https://doi.org/10.1890/120150, 2013.

Båserud, L., Reuder, J., Jonassen, M. O., Kral, S. T., Paskyabi, M. B., and Lothon, M.: Proof of concept for turbulence measurements with the RPAS SUMO during the BLLAST campaign, Atmos. Meas. Tech., 9, 4901-4913, 10.5194/amt-9-4901-2016, 2016.

Billesbach, D. P.: Estimating uncertainties in individual eddy covariance flux measurements: A comparison of methods and a proposed new method, Agricultural and Forest Meteorology, 151, 394-405, https://doi.org/10.1016/j.agrformet.2010.12.001, 2011.

Calmer, R., Roberts, G. C., Sanchez, K. J., Sciare, J., Sellegri, K., Picard, D., Vrekoussis, M., and Pikridas, M.: Aerosol–cloud closure study on cloud optical properties using remotely piloted aircraft measurements during a BACCHUS field campaign in Cyprus, Atmos. Chem. Phys., 19, 13989-14007, 10.5194/acp-19-13989-2019, 2019.

Chandra, N., Patra, P. K., Niwa, Y., Ito, A., Iida, Y., Goto, D., Morimoto, S., Kondo, M., Takigawa, M., Hajima, T., and Watanabe, M.: Estimated regional CO_2 flux and uncertainty based on an ensemble of atmospheric CO_2 inversions, Atmos. Chem. Phys., 22, 9215-9243, 10.5194/acp-22-9215-2022, 2022.

Chen, J. M., Leblanc, S. G., Cihlar, J., Desjardins, R. L., and MacPherson, J. I.: Extending aircraft- and tower-based CO_2 flux measurements to a boreal region using a Landsat thematic mapper land cover map, Journal of Geophysical Research: Atmospheres, 104, 16859-16877, https://doi.org/10.1029/1999JD900129, 1999.

814   Chen, W., Wang, D., Huang, Y., Chen, L., Zhang, L., Wei, X., Sang, M., Wang, F., Liu, J., and Hu, B.: Monitoring and analysis
815   of coastal reclamation from 1995–2015 in Tianjin Binhai New Area, China, Scientific Reports, 7, 3850, 10.1038/s41598-017-
816   04155-0, 2017.

817   Chu, H., Luo, X., Ouyang, Z., Chan, W. S., Dengel, S., Biraud, S. C., Torn, M. S., Metzger, S., Kumar, J., Arain, M. A.,
818   Arkebauer, T. J., Baldocchi, D., Bernacchi, C., Billesbach, D., Black, T. A., Blanken, P. D., Bohrer, G., Bracho, R., Brown,
819   S., Brunsell, N. A., Chen, J., Chen, X., Clark, K., Desai, A. R., Duman, T., Durden, D., Fares, S., Forbrich, I., Gamon, J. A.,
820   Gough, C. M., Griffis, T., Helbig, M., Hollinger, D., Humphreys, E., Ikawa, H., Iwata, H., Ju, Y., Knowles, J. F., Knox, S. H.,
821   Kobayashi, H., Kolb, T., Law, B., Lee, X., Litvak, M., Liu, H., Munger, J. W., Noormets, A., Novick, K., Oberbauer, S. F.,
822   Oechel, W., Oikawa, P., Papuga, S. A., Pendall, E., Prajapati, P., Prueger, J., Quinton, W. L., Richardson, A. D., Russell, E.
823   S., Scott, R. L., Starr, G., Staebler, R., Stoy, P. C., Stuart-Haëntjens, E., Sonnentag, O., Sullivan, R. C., Suyker, A., Ueyama,
824   M., Vargas, R., Wood, J. D., and Zona, D.: Representativeness of Eddy-Covariance flux footprints for areas surrounding
825   AmeriFlux sites, Agricultural and Forest Meteorology, 301-302, 108350, https://doi.org/10.1016/j.agrformet.2021.108350,
826   2021.

827   Crawford, T. L. and Dobosy, R. J.: A sensitive fast-response probe to measure turbulence and heat flux from any airplane,
828   Boundary-Layer Meteorology, 59, 257-278, 10.1007/BF00119816, 1992.

829   Crawford, T. L., Dobosy, R. J., and Dumas, E. J.: Aircraft wind measurement considering lift-induced upwash, Boundary-
830   Layer Meteorology, 80, 79-94, 10.1007/BF00119012, 1996.

831   Desjardins, R. L., Brach, E. J., Alvo, P., and Schuepp, P. H.: Aircraft Monitoring of Surface Carbon Dioxide Exchange, Science,
832   216, 733-735, 10.1126/science.216.4547.733, 1982.

833   Desjardins, R. L., Worth, D. E., MacPherson, J. I., Bastian, M., and Srinivasan, R.: Flux measurements by the NRC Twin Otter
834   atmospheric research aircraft: 1987–2011, Adv. Sci. Res., 13, 43-49, 10.5194/asr-13-43-2016, 2016.

835   Drüe, C. and Heinemann, G.: A Review and Practical Guide to In-Flight Calibration for Aircraft Turbulence Sensors, Journal
836   of Atmospheric and Oceanic Technology, 30, 2820-2837, 10.1175/JTECH-D-12-00103.1, 2013.

837   Elston, J., Argrow, B., Stachura, M., Weibel, D., Lawrence, D., and Pope, D.: Overview of Small Fixed-Wing Unmanned
838   Aircraft for Meteorological Sampling, Journal of Atmospheric and Oceanic Technology, 32, 97-115, 10.1175/JTECH-D-13-
839   00236.1, 2015.

840   Enriquez, A. G. and Friehe, C. A.: Effects of Wind Stress and Wind Stress Curl Variability on Coastal Upwelling, Journal of
841   Physical Oceanography, 25, 1651-1671, https://doi.org/10.1175/1520-0485(1995)025<1651:EOWSAW>2.0.CO;2, 1995.

842   Finkelstein, P. L. and Sims, P. F.: Sampling error in eddy correlation flux measurements, Journal of Geophysical Research:
843   Atmospheres, 106, 3503-3509, https://doi.org/10.1029/2000JD900731, 2001.

844   Garman, K. E., Wyss, P., Carlsen, M., Zimmerman, J. R., Stirm, B. H., Carney, T. Q., Santini, R., and Shepson, P. B.: The
845   Contribution of Variability of Lift-induced Upwash to the Uncertainty in Vertical Winds Determined from an Aircraft Platform,
846   Boundary-Layer Meteorology, 126, 461-476, 10.1007/s10546-007-9237-y, 2008.

847 Garman, K. E., Hill, K. A., Wyss, P., Carlsen, M., Zimmerman, J. R., Stirm, B. H., Carney, T. Q., Santini, R., and Shepson, P.
848 B.: An Airborne and Wind Tunnel Evaluation of a Wind Turbulence Measurement System for Aircraft-Based Flux
849 Measurements, Journal of Atmospheric and Oceanic Technology, 23, 1696-1708, 10.1175/JTECH1940.1, 2006.

850 Gioli, B., Miglietta, F., Vaccari, F. P., and Zaldei, A.: The Sky Arrow ERA, an innovative airborne platform to monitor mass,
851 momentum and energy exchange of ecosystems, Annals of Geophysics, 49, 109-116, 10.4401/ag-3159, 2006.

852 Gioli, B., Miglietta, F., De Martino, B., Hutjes, R. W. A., Dolman, H. A. J., Lindroth, A., Schumacher, M., Sanz, M. J., Manca,
853 G., Peressotti, A., and Dumas, E. J.: Comparison between tower and aircraft-based eddy covariance fluxes in five European
854 regions, Agricultural and Forest Meteorology, 127, 1-16, https://doi.org/10.1016/j.agrformet.2004.08.004, 2004.

855 Hannun, R. A., Wolfe, G. M., Kawa, S. R., Hanisco, T. F., Newman, P. A., Alfieri, J. G., Barrick, J., Clark, K. L., DiGangi, J.
856 P., Diskin, G. S., King, J., Kustas, W. P., Mitra, B., Noormets, A., Nowak, J. B., Thornhill, K. L., and Vargas, R.: Spatial
857 heterogeneity in CO2, CH4, and energy fluxes: insights from airborne eddy covariance measurements over the Mid-Atlantic
858 region, Environmental Research Letters, 15, 035008, 10.1088/1748-9326/ab7391, 2020.

859 Hu, G. and Jia, L.: Monitoring of Evapotranspiration in a Semi-Arid Inland River Basin by Combining Microwave and Optical
860 Remote Sensing Observations, Remote Sensing, 7, 10.3390/rs70303056, 2015.

861 Kaimal, J. C., Clifford, S. F., and Lataitis, R. J.: Effect of finite sampling on atmospheric spectra, Boundary-Layer Meteorology,
862 47, 337-347, 10.1007/BF00122338, 1989.

863 Kalogiros, J. A. and Wang, Q.: Aerodynamic Effects on Wind Turbulence Measurements with Research Aircraft, Journal of
864 Atmospheric and Oceanic Technology, 19, 1567-1576, 10.1175/1520-0426(2002)019<1567:AEOWTM>2.0.CO;2, 2002.

865 Khelif, D., Burns, S. P., and Friehe, C. A.: Improved Wind Measurements on Research Aircraft, Journal of Atmospheric and
866 Oceanic Technology, 16, 860-875, 10.1175/1520-0426(1999)016<0860:IWMORA>2.0.CO;2, 1999.

867 Kowalski, A. S., Serrano-Ortiz, P., Miranda-García, G., and Fratini, G.: Disentangling Turbulent Gas Diffusion from Non-
868 diffusive Transport in the Boundary Layer, Boundary-Layer Meteorology, 179, 347-367, 10.1007/s10546-021-00605-5, 2021.

869 Lenschow, D. H.: Aircraft Measurements in the Boundary Layer, in: Probing the Atmospheric Boundary Layer, edited by:
870 Lenschow, D. H., American Meteorological Society, Boston, MA, Boston, https://doi.org/10.1007/978-1-944970-14-7_5,
871 1986.

872 Lenschow, D. H. and Sun, J.: The spectral composition of fluxes and variances over land and sea out to the mesoscale,
873 Boundary-Layer Meteorology, 125, 63-84, 10.1007/s10546-007-9191-8, 2007.

874 Lenschow, D. H., Delany, A. C., Stankov, B. B., and Stedman, D. H.: Airborne measurements of the vertical flux of ozone in
875 the boundary layer, Boundary-Layer Meteorology, 19, 249-265, 10.1007/BF00117223, 1980.

876 Li, X., Liu, S., Xiao, Q., Ma, M., Jin, R., Che, T., Wang, W., Hu, X., Xu, Z., Wen, J., and Wang, L.: A multiscale dataset for
877 understanding complex eco-hydrological processes in a heterogeneous oasis system, Scientific Data, 4, 170083,
878 10.1038/sdata.2017.83, 2017.

879 Li, X., Liu, S., Yang, X., Ma, Y., He, X., Xu, Z., Xu, T., Song, L., Zhang, Y., Hu, X., Ju, Q., and Zhang, X.: Upscaling
880 Evapotranspiration from a Single-Site to Satellite Pixel Scale, 10.3390/rs13204072, 2021.

881 Li, X., Liu, S., Li, H., Ma, Y., Wang, J., Zhang, Y., Xu, Z., Xu, T., Song, L., Yang, X., Lu, Z., Wang, Z., and Guo, Z.:
882 Intercomparison of Six Upscaling Evapotranspiration Methods: From Site to the Satellite Pixel, Journal of Geophysical
883 Research: Atmospheres, 123, 6777-6803, https://doi.org/10.1029/2018JD028422, 2018.

884 Liu, H., Randerson, J. T., Lindfors, J., Massman, W. J., and Foken, T.: Consequences of Incomplete Surface Energy Balance
885 Closure for CO2 Fluxes from Open-Path CO2/H2O Infrared Gas Analysers, Boundary-Layer Meteorology, 120, 65-85,
886 10.1007/s10546-005-9047-z, 2006.

887 Liu, J., Chen, J. M., Cihlar, J., and Chen, W.: Net primary productivity distribution in the BOREAS region from a process
888 model using satellite and surface data, Journal of Geophysical Research: Atmospheres, 104, 27735-27754,
889 https://doi.org/10.1029/1999JD900768, 1999.

890 Liu, S., Xu, Z., Song, L., Zhao, Q., Ge, Y., Xu, T., Ma, Y., Zhu, Z., Jia, Z., and Zhang, F.: Upscaling evapotranspiration
891 measurements from multi-site to the satellite pixel scale over heterogeneous land surfaces, Agricultural and Forest
892 Meteorology, 230-231, 97-113, https://doi.org/10.1016/j.agrformet.2016.04.008, 2016.

893 Liu, S., Li, X., Xu, Z., Che, T., Xiao, Q., Ma, M., Liu, Q., Jin, R., Guo, J., Wang, L., Wang, W., Qi, Y., Li, H., Xu, T., Ran,
894 Y., Hu, X., Shi, S., Zhu, Z., Tan, J., Zhang, Y., and Ren, Z.: The Heihe Integrated Observatory Network: A Basin-Scale Land
895 Surface Processes Observatory in China, Vadose Zone Journal, 17, 180072, https://doi.org/10.2136/vzj2018.04.0072, 2018.

896 Mahrt, L.: Flux Sampling Errors for Aircraft and Towers, Journal of Atmospheric and Oceanic Technology, 15, 416-429,
897 https://doi.org/10.1175/1520-0426(1998)015<0416:FSEFAA>2.0.CO;2, 1998.

898 Massman, W. and Clement, R.: Uncertainty in Eddy Covariance Flux Estimates Resulting from Spectral Attenuation, in:
899 Handbook of Micrometeorology: A Guide for Surface Flux Measurement and Analysis, edited by: Lee, X., Massman, W., and
900 Law, B., Springer Netherlands, Dordrecht, 67-99, 10.1007/1-4020-2265-4_4, 2005.

901 Mathez, E. and Smerdon, J.: Climate Change3. Ocean– Atmosphere Interactions, in: The Science of Global Warming and Our
902 Energy Future, Columbia University Press, 69-100, doi:10.7312/math17282-005, 2018.

903 Mauder, M., Cuntz, M., Drüe, C., Graf, A., Rebmann, C., Schmid, H. P., Schmidt, M., and Steinbrecher, R.: A strategy for
904 quality and uncertainty assessment of long-term eddy-covariance measurements, Agricultural and Forest Meteorology, 169,
905 122-135, https://doi.org/10.1016/j.agrformet.2012.09.006, 2013.

906 Mayer, J., Mayer, M., Haimberger, L., and Liu, C.: Comparison of Surface Energy Fluxes from Global to Local Scale, Journal
907 of Climate, 35, 4551-4569, 10.1175/JCLI-D-21-0598.1, 2022.

908 Metzger, S., Junkermann, W., Butterbach-Bahl, K., Schmid, H. P., and Foken, T.: Measuring the 3-D wind vector with a
909 weight-shift microlight aircraft, Atmos. Meas. Tech., 4, 1421-1444, 10.5194/amt-4-1421-2011, 2011.

910 Metzger, S., Junkermann, W., Mauder, M., Beyrich, F., Butterbach-Bahl, K., Schmid, H. P., and Foken, T.: Eddy-covariance
911 flux measurements with a weight-shift microlight aircraft, Atmos. Meas. Tech., 5, 1699-1717, 10.5194/amt-5-1699-2012, 2012.

912 Mohan, M. M. P., Rajitha, K., and Murari, R. R. V.: Review of approaches for the estimation of sensible heat flux in remote
913 sensing-based evapotranspiration models, Journal of Applied Remote Sensing, 14, 1-31, 10.1117/1.JRS.14.041501, 2020.

914 Peltola, O., Aslan, T., Ibrom, A., Nemitz, E., Rannik, Ü., and Mammarella, I.: The high-frequency response correction of eddy
915 covariance fluxes – Part 1: An experimental approach and its interdependence with the time-lag estimation, Atmos. Meas.
916 Tech., 14, 5071-5088, 10.5194/amt-14-5071-2021, 2021.

917 Prudden, S., Fisher, A., Marino, M., Mohamed, A., Watkins, S., and Wild, G.: Measuring wind with Small Unmanned Aircraft
918 Systems, Journal of Wind Engineering and Industrial Aerodynamics, 176, 197-210,
919 https://doi.org/10.1016/j.jweia.2018.03.029, 2018.

920 Prueger, J. H., Hatfield, J. L., Parkin, T. B., Kustas, W. P., Hipps, L. E., Neale, C. M. U., MacPherson, J. I., Eichinger, W. E.,
921 and Cooper, D. I.: Tower and Aircraft Eddy Covariance Measurements of Water Vapor, Energy, and Carbon Dioxide Fluxes
922 during SMACEX, Journal of Hydrometeorology, 6, 954-960, 10.1175/JHM457.1, 2005.

923 Rannik, Ü., Peltola, O., and Mammarella, I.: Random uncertainties of flux measurements by the eddy covariance technique,
924 Atmos. Meas. Tech., 9, 5163-5181, 10.5194/amt-9-5163-2016, 2016.

925 Reineman, B. D., Lenain, L., Statom, N. M., and Melville, W. K.: Development and Testing of Instrumentation for UAV-
926 Based Flux Measurements within Terrestrial and Marine Atmospheric Boundary Layers, Journal of Atmospheric and Oceanic
927 Technology, 30, 1295-1319, 10.1175/JTECH-D-12-00176.1, 2013.

928 Reuder, J., Båserud, L., Jonassen, M. O., Kral, S. T., and Müller, M.: Exploring the potential of the RPA system SUMO for
929 multipurpose boundary-layer missions during the BLLAST campaign, Atmos. Meas. Tech., 9, 2675-2688, 10.5194/amt-9-
930 2675-2016, 2016.

931 Reuter, M., Bovensmann, H., Buchwitz, M., Borchardt, J., Krautwurst, S., Gerilowski, K., Lindauer, M., Kubistin, D., and
932 Burrows, J. P.: Development of a small unmanned aircraft system to derive CO_2 emissions of anthropogenic point sources,
933 Atmos. Meas. Tech., 14, 153-172, 10.5194/amt-14-153-2021, 2021.

934 Serrano-Ortiz, P., Kowalski, A. S., Domingo, F., Ruiz, B., and Alados-Arboledas, L.: Consequences of Uncertainties in CO_2
935 Density for Estimating Net Ecosystem CO_2 Exchange by Open-path Eddy Covariance, Boundary-Layer Meteorology, 126,
936 209-218, 10.1007/s10546-007-9234-1, 2008.

937 Sun, Y., Jia, L., Chen, Q., and Zheng, C.: Optimizing Window Length for Turbulent Heat Flux Calculations from Airborne
938 Eddy Covariance Measurements under Near Neutral to Unstable Atmospheric Stability Conditions, Remote Sensing, 10,
939 10.3390/rs10050670, 2018.

940 Sun, Y., Ma, J., Sude, B., Lin, X., Shang, H., Geng, B., Diao, Z., Du, J., and Quan, Z.: A UAV-Based Eddy Covariance System
941 for Measurement of Mass and Energy Exchange of the Ecosystem: Preliminary Results, Sensors, 21, 10.3390/s21020403,
942 2021a.

943 Sun, Y., Sude, B., Geng, B., Ma, J., Lin, X., Hao, Z., Jing, W., Chen, Q., and Quan, Z.: Observation of the winter regional
944 evaporative fraction using a UAV-based eddy covariance system over wetland area, Agricultural and Forest Meteorology, 310,
945 108619, https://doi.org/10.1016/j.agrformet.2021.108619, 2021b.

946 Tadić, J. M., Miller, S., Yadav, V., and Biraud, S. C.: Greenhouse gas fluxes from Alaska's North Slope inferred from the
947 Airborne Carbon Measurements campaign (ACME-V), Atmospheric Environment, 248, 118239,
948 https://doi.org/10.1016/j.atmosenv.2021.118239, 2021.

949 Thomas, R. M., Lehmann, K., Nguyen, H., Jackson, D. L., Wolfe, D., and Ramanathan, V.: Measurement of turbulent water
950 vapor fluxes using a lightweight unmanned aerial vehicle system, Atmos. Meas. Tech., 5, 243-257, 10.5194/amt-5-243-2012,
951 2012.

952 van den Kroonenberg, A., Martin, T., Buschmann, M., Bange, J., and Vörsmann, P.: Measuring the Wind Vector Using the
953 Autonomous Mini Aerial Vehicle M2AV, Journal of Atmospheric and Oceanic Technology, 25, 1969-1982,
954 10.1175/2008JTECHA1114.1, 2008.

955 Vellinga, O. S., Dobosy, R. J., Dumas, E. J., Gioli, B., Elbers, J. A., and Hutjes, R. W. A.: Calibration and Quality Assurance
956 of Flux Observations from a Small Research Aircraft*, Journal of Atmospheric and Oceanic Technology, 30, 161-181,
957 10.1175/JTECH-D-11-00138.1, 2013.

958 Wang, H., Jia, G., Zhang, A., and Miao, C.: Assessment of Spatial Representativeness of Eddy Covariance Flux Data from
959 Flux Tower to Regional Grid, Remote Sensing, 8, 742, 2016.

960 Webb, E. K., Pearman, G. I., and Leuning, R.: Correction of flux measurements for density effects due to heat and water
961 vapour transfer, Quarterly Journal of the Royal Meteorological Society, 106, 85-100, https://doi.org/10.1002/qj.49710644707,
962 1980.

963 Williams, A. and Marcotte, D.: Wind Measurements on a Maneuvering Twin-Engine Turboprop Aircraft Accounting for Flow
964 Distortion, Journal of Atmospheric and Oceanic Technology, 17, 795-810, 10.1175/1520-
965 0426(2000)017<0795:WMOAMT>2.0.CO;2, 2000.

966 Witte, B. M., Singler, R. F., and Bailey, S. C. C.: Development of an Unmanned Aerial Vehicle for the Measurement of
967 Turbulence in the Atmospheric Boundary Layer, Atmosphere, 8, 10.3390/atmos8100195, 2017.

968 Wolfe, G. M., Kawa, S. R., Hanisco, T. F., Hannun, R. A., Newman, P. A., Swanson, A., Bailey, S., Barrick, J., Thornhill, K.
969 L., Diskin, G., DiGangi, J., Nowak, J. B., Sorenson, C., Bland, G., Yungel, J. K., and Swenson, C. A.: The NASA Carbon
970 Airborne Flux Experiment (CARAFE): instrumentation and methodology, Atmos. Meas. Tech., 11, 1757-1776, 10.5194/amt-
971 11-1757-2018, 2018.

972 Xu, S., Xu, S., Zhou, Y., Yue, S., Zhang, X., Gu, R., Zhang, Y., Qiao, Y., and Liu, M.: Long-Term Changes in the Unique and
973 Largest Seagrass Meadows in the Bohai Sea (China) Using Satellite (1974–2019) and Sonar Data: Implication for Conservation
974 and Restoration, Remote Sensing, 13, 856, 10.3390/rs13050856, 2021.

975 Yang, X., Yong, B., Ren, L., Zhang, Y., and Long, D.: Multi-scale validation of GLEAM evapotranspiration products over
976 China via ChinaFLUX ET measurements, International Journal of Remote Sensing, 38, 5688-5709,
977 10.1080/01431161.2017.1346400, 2017.

978 Zappa, C. J., Brown, S. M., Laxague, N. J. M., Dhakal, T., Harris, R. A., Farber, A. M., and Subramaniam, A.: Using Ship-
979 Deployed High-Endurance Unmanned Aerial Vehicles for the Study of Ocean Surface and Atmospheric Boundary Layer
980 Processes, Frontiers in Marine Science, 6, 10.3389/fmars.2019.00777, 2020.

981 Zhang, G., Zhang, J., and Meng, P.: Estimation of kilometer-scale heat fluxes over a hilly area in Northern China using an
982 optical-microwave scintillometer, Agricultural Water Management, 244, 106582,
983 https://doi.org/10.1016/j.agwat.2020.106582, 2021.

984 Zheng, C., Liu, S., Song, L., Xu, Z., Guo, J., Ma, Y., Ju, Q., and Wang, J.: Comparison of sensible and latent heat fluxes from
985 optical-microwave scintillometers and eddy covariance systems with respect to surface energy balance closure, Agricultural
986 and Forest Meteorology, 331, 109345, https://doi.org/10.1016/j.agrformet.2023.109345, 2023.

987